

REPORT DOCUMENTATION PAGE				Form Approved OMB No. 0704-0188	
The public reporting burden for this collection of information is estimated to average 1 hour per response, including the time for reviewing instructions, searching existing data sources, gathering and maintaining the data needed, and completing and reviewing the collection of information. Send comments regarding this burden estimate or any other aspect of this collection of information, including suggestions for reducing the burden, to Department of Defense, Washington Headquarters Services, Directorate for Information Operations and Reports (0704-0188), 1215 Jefferson Davis Highway, Suite 1204, Arlington, VA 22202-4302. Respondents should be aware that notwithstanding any other provision of law, no person shall be subject to any penalty for failing to comply with a collection of information if it does not display a currently valid OMB control number.					
1. REPORT DATE (DD-MM-YYYY) 25-07-2001		2. REPORT TYPE FINAL REPORT		3. DATES COVERED (From - To) Feb 2001 - Jul 2001	
4. TITLE AND SUBTITLE A Theoretical and Experimental Investigation of Acoustic Dyadic Sensors				5a. CONTRACT NUMBER N00014 - 01 - M - 0077	
				5b. GRANT NUMBER N/A	
				5c. PROGRAM ELEMENT NUMBER N/A	
				5d. PROJECT NUMBER N/A	
6. AUTHOR(S) Silvia, Manuel T.				5e. TASK NUMBER N/A	
				5f. WORK UNIT NUMBER N/A	
7. PERFORMING ORGANIZATION NAME(S) AND ADDRESS(ES) SITTEL CORPORATION Research and Development Department 1206 Foothill Road Ojai, CA 93023-1727				8. PERFORMING ORGANIZATION REPORT NUMBER SITTEL Technical Report TP 4	
9. SPONSORING/MONITORING AGENCY NAME(S) AND ADDRESS(ES) Office of Naval Research Ballston Tower One 800 North Quincy Street Arlington, VA 22217-5660				10. SPONSOR/MONITOR'S ACRONYM(S) ONR	
				11. SPONSOR/MONITOR'S REPORT NUMBER(S) N/A	
12. DISTRIBUTION/AVAILABILITY STATEMENT Approved For Public Release; Distribution is Unlimited					
13. SUPPLEMENTARY NOTES None					
14. ABSTRACT This report sets the groundwork for a generalized theory of directional sensors using the Taylor series of the acoustic pressure; it moves from the basic pressure sensor to the vector sensor, on to the dyadic sensor, then on to higher-order sensors depending on the number of terms in the Taylor series. A benefit of higher-order sensors is improvement in the 3-dB beamwidth; 105 degrees for a vector sensor, 65 degrees for a dyadic sensor. An analysis shows (i) how finite-difference approximations can be utilized to estimate the 10 terms that define the dyadic sensor, (ii) it is not prudent to employ finite differences to the estimation of 2nd-order partial derivatives of the pressure, (iii) a dyadic sensor be realized with 18 accelerometers and a pressure sensor and (iv) that this realization requires only 1st-order finite differences, which can be performed in the presence quantization and wide band noise effects. A partial dyadic sensor (three orthogonal accelerometer dipoles and a pressure sensor at the origin) was tested at Seneca Lake during May 2001. The experimental in-water beam pattern measurements confirmed theoretical predictions.					
15. SUBJECT TERMS Directional acoustic sensors, scalar sensors, vector sensors, dyadic sensors, Taylor series, Finite-difference approximations, accelerometers, hydrophones,					
16. SECURITY CLASSIFICATION OF:			17. LIMITATION OF ABSTRACT		18. NUMBER OF PAGES
a. REPORT U	b. ABSTRACT U	c. THIS PAGE U	UU		47
19a. NAME OF RESPONSIBLE PERSON Dr. Manuel T. Silvia					19b. TELEPHONE NUMBER (Include area code) (805) 646-0700

20010824 095

Office of Naval Research

Contract Number: N00014-01-M-0077

Contract Data Line Requirement Number: A001

FINAL REPORT

Report Title: A Theoretical and Experimental Investigation of Acoustic Dyadic Sensors

Date of Report: July 25, 2001

SITTEL CORPORATION  
Ojai, California

Distribution:

Per Enclosure Number 1

SITTEL Technical Report TP 4  
July 25, 2001

# **A THEORETICAL AND EXPERIMENTAL INVESTIGATION OF ACOUSTIC DYADIC SENSORS**

**MANUEL T. SILVIA**  
**RESEARCH AND DEVELOPMENT DEPARTMENT**

The logo for Sittel, featuring the word "Sittel" in a stylized, blackletter-style font.

**SITTEL CORPORATION**  
**OJAI, CALIFORNIA**

## PREFACE

Though this report, as per its title, deals primarily with the theoretical and experimental investigation of acoustic dyadic sensors, it sets the groundwork for a generalized theory of directional acoustic sensors. Starting with the Taylor series of the acoustic pressure, it moves quickly from the basic pressure sensor to the vector sensor and then on to the dyadic sensor. More generalized acoustic sensors are obtained by including additional terms of the Taylor series. One of the payoffs of more advanced sensors is improvement in the beamwidth. With a vector sensor, we can achieve a beamwidth of  $105^\circ$  from a single point. Using an acoustic dyadic sensor, this beamwidth can be decreased to  $65^\circ$ . A further reduction in beamwidth is anticipated as the order of the acoustic sensor increases (achieved by the addition of more Taylor series terms).

This report shows how finite-difference approximations can be utilized to estimate the 10 terms that define the dyadic sensor. The associated realization of the dyadic sensor takes on the form of 19 judiciously placed pressure sensors. An alternative realization using 18 accelerometers and 1 pressure sensor is also considered. Both realizations involve a symmetrical placement of sensors, which allows us to consider the sensors as collocated with a common phase center at the origin. A detailed analysis is carried out in this report of the error that arises when using finite differences in an environment of mismatched sensors that have nonzero spacing between them. The analysis shows that it is not prudent to employ the method of finite differences to the estimation of second-order partial derivatives of the pressure. The opposite is true for the estimation of first-order partial derivatives (the gradient of the pressure). For example, for a  $\pm 0.2$  dB amplitude mismatch and a one-tenth of wavelength spacing, a typical mean error in estimating a first-order partial is about  $-0.14$  dB with a standard deviation of about  $0.06$  dB. The error analysis leads to the recommendation that an acoustic dyadic sensor be realized with 18 accelerometers and a pressure sensor at the origin. This will eliminate the gradient estimation error and significantly reduce the Hessian estimation error, since the Hessian of the pressure can now be estimated by first-order finite-difference approximations.

This report also shows that these first-order finite-difference approximations can be successfully performed in the presence of quantization and wide band noise effects. A worst-case analysis shows that using two accelerometers spaced 3 inches apart, one can achieve a normalized RMS error of 10% when attempting a first-order finite difference of a 50 Hz plane wave in a 2000 Hz band. This requires a signal-to-noise ratio (SNR) of at least 30 dB and assumes that the noise at each accelerometer is uncorrelated. This can be done using a 16-bit analog-to-digital converter (ADC). Further, for frequencies up to 2000 Hz, the required SNR drops off at about 6 dB per octave. This implies that the same 3-inch spaced accelerometers only need a SNR of 6 dB to achieve the same 10 % error for a first-order finite difference of a 800Hz plane wave.

A partial dyadic sensor (three orthogonal accelerometer dipoles and a pressure sensor at the origin) was tested at Seneca Lake during May 2001. The experimental in-water beam pattern measurements confirmed theoretical predictions. SITTEL CORPORATION also demonstrated that for a plane wave source, dyadic sensor performance can be achieved by advanced signal processing of only the pressure and acceleration measurements.

This report was prepared for James McEachern and his ONR 321SS team under ONR contract number N00014-01-M-007. The Program Officer was Jan Lindberg. This is the Final Report and is submitted in accordance with CDRL A001, Item number 0001AA- Final Report.

**SITTEL Technical Report TP 4**  
**July 25, 2001**

**FINAL REPORT**

**A THEORETICAL AND EXPERIMENTAL INVESTIGATION  
OF ACOUSTIC DYADIC SENSORS**

**Submitted to**

**Office of Naval Research  
Dr. Jan Lindberg (Code 321SS)  
Ballston Centre Tower One  
800 North Quincy Street  
Arlington, VA 22217-5660**

**By**

**SITTEL CORPORATION  
Dr. Manuel T. Silvia  
1206 Foothill Road  
Ojai, CA 93023-1727**

**In accordance with**

**CDRL A001, Item Number 0001AA of ONR Contract No. N00014-01-M-0077**

**July 25, 2001**

# TABLE OF CONTENTS

	Page
LIST OF ILLUSTRATIONS.....	ii
1.0 INTRODUCTION.....	1
2.0 GENERAL THEORY OF DIRECTIONAL ACOUSTIC SENSORS.....	1
3.0 REALIZATION OF AN ACOUSTIC DYADIC SENSOR.....	5
4.0 ANALYSIS OF A THEORETICAL ACOUSTIC DYADIC SENSOR.....	10
5.0 MULTI-CHANNEL FILTERING AND DIRECTIONAL ACOUSTIC SENSORS.....	23
6.0 EXPERIMENTAL RESULTS USING A PARTIAL DYADIC SENSOR.....	27
7.0 EFFECTS OF QUANTIZATION AND WIDE BAND NOISE ON THE FINITE DIFFERENCES BETWEEN TWO ACCELEROMETERS.....	36
8.0 SUMMARY AND RECOMMENDATIONS FOR FUTURE RESEARCH.....	43
APPENDIX A.....	A-1
REFERENCES.....	R-1

## LIST OF ILLUSTRATIONS

Figure		Page
1	The propagation of a planar wave-front toward the origin of a rectangular coordinate system.....	4
2	Normalized mean-squared estimation error (equation (19)) vs. $R/\lambda$ .....	4
3	Spherical coverage for 10% error.....	5
4	The arrangement of six pressure sensors for the finite-difference the pressure approximation of the gradient.....	6
5	Sensor placement for the estimation of the diagonal elements of the Hessian of the pressure at the origin.....	7
6	Sensor placement for the estimation of the off-diagonal elements of the Hessian of the pressure at the origin.....	8
7	The error $\mathcal{E}$ in estimating the partial derivative of the pressure with respect to $x$ (at the origin). $\phi_T = 90^\circ$ and $\theta_T = 0^\circ$ .....	12
8	Relationship between percent error and dB error.....	12
9	Contour plot of the error $\mathcal{E}$ as a function of $\mu$ and $\Delta x/\lambda$ for the case $n_n = \pm 1$ .....	14
10	A contour plot of the error $\mathcal{E}$ for the case $n_x = \pm \frac{1}{2}$ .....	15
11	Arrangement of pressure sensors for the finite-difference approximation of the pure second-order partial $\partial^2 p/\partial x^2$ at the origin.....	15
12	Contour plot for $\mathcal{E}$ as a function of the mismatch parameters $\mu_2$ and $\mu_3$ for the special case of $\phi_T = 90^\circ$ , $\theta_T = 0^\circ$ and $\Delta x/\lambda = 0.118$ .....	17
13	Arrangement of pressure sensors for the finite-difference approximation of the mixed second-order partial $\partial^2 p/\partial x \partial y$ at the origin.....	18
14	Error $\mathcal{E}$ with $\text{dB}_{\max}$ going from 0.1 to 2 dB in steps of 0.1 dB and $\phi_T = 90^\circ$ and $\theta_T = 45^\circ$ .....	20
15	Error $\mathcal{E}$ with $\text{dB}_{\max}$ of 0.5, 1.0, 1.5, and 2.0 dB and $\phi_T = 90^\circ$ , $\theta_T = 45^\circ$ ...	20

## LIST OF ILLUSTRATIONS (Cont'd)

Figure		Page
16	Statistical behavior of the error in estimating the mixed second-order partial derivative (with respect to $x$ and $y$ ) at the origin.....	22
17	Statistics of the error in estimating the first-order (shown at the left) and pure second-order (shown at the right) partial derivatives of the pressure at the origin.....	22
18	Polar plots of the normalized Taylor approximation error as a function of $\theta_S$ for $\phi_S = \phi_T = 90^\circ$ and $\theta_T = 0^\circ$ and several values of $r/\lambda$ .....	24
19	Multi-channel Filtering and Directional Acoustic Sensors.....	25
20	Selection of weights for a vector sensor. (a) For maximum array gain. (b) For optimum null placement.....	26
21	Selection of weights for a dyadic sensor. (a) For maximum array gain. (b) For optimum null placement.....	26
22	Partial dyadic sensor built by EDO Electro-Ceramic Products.....	27
23	Support structure used for partial dyadic sensor.....	28
24	Empirical and theoretical beam patterns. (a) +x accelerometer (b) -x accelerometer (c) the difference between the +x and -x accels.....	29
25	Empirical and theoretical beam patterns. (a) +y accelerometer (b) -y accelerometer (c) the difference between the +y and -y accels.....	29
26	FRAZ display using vector sensor processing (single 400 Hz target located at $r = 130$ ft, $\theta_T = 0^\circ$ , $\phi_T = 90^\circ$ ).....	34
27	FRAZ display using dyadic sensor processing (single 400 Hz target located at $r = 130$ ft, $\theta_T = 0^\circ$ , $\phi_T = 90^\circ$ ).....	34
28.	FRAZ display using vector sensor processing (400 Hz target located at $r = 130$ ft, $\theta_T = 0^\circ$ , $\phi_T = 90^\circ$ and 1300 Hz interferer located at $r_I = 222$ ft, $\theta_I = 225^\circ$ , $\phi_I = 19^\circ$ ).....	35
29	FRAZ display using dyadic sensor processing (400 Hz target located at $r = 130$ ft, $\theta_T = 0^\circ$ , $\phi_T = 90^\circ$ , and 1300 Hz interferer located at $r_I = 222$ ft, $\theta_I = 225^\circ$ , $\phi_I = 19^\circ$ ).....	35



## LIST OF ILLUSTRATIONS (Cont'd)

Figure		Page
30.	Modeling Setup.....	36
31.	Average MSE with 16 Bit ADC, 3 Inch Accelerometer Spacing.....	41
32.	Maximum MSE with 16 Bit ADC, 3 Inch Accelerometer Spacing.....	41
33.	Average MSE with 24 Bit ADC, 3 Inch Accelerometer Spacing.....	41
34.	Maximum MSE with 24 Bit ADC, 3 Inch Accelerometer Spacing.....	41
35.	Average MSE with 16 Bit ADC, 6 Inch Accelerometer Spacing.....	41
36.	Maximum MSE with 16 Bit ADC, 6 Inch Accelerometer Spacing.....	41
37.	Average MSE with 16 Bit ADC, 3-Inch Accelerometer Spacing, and an average of 2 Accelerometer sets.....	42
38.	Maximum MSE with 16 Bit ADC, 3-Inch Accelerometer Spacing, and an average of 2 Accelerometer sets.....	42
39.	Average MSE with 16 Bit ADC as a Function of Noise Correlation.....	42
40.	Maximum MSE with 16 Bit ADC as a Function of Noise Correlation.....	42
41.	Average MSE with 16 Bit ADC and 3 Inch Accelerometer Spacing, as a function of frequency.....	42
42.	Maximum MSE with 24 Bit ADC and 3 Inch Accelerometer Spacing, as a function of frequency.....	42

# A Theoretical and Experimental Investigation Of Acoustic Dyadic Sensors

## 1.0 Introduction

Current research in the area of directional acoustic sensors has shown that a tri-axial accelerometer and an omnidirectional hydrophone, packaged in the same housing with a common acoustic phase center, can provide an effective directional acoustic sensor [1,2,3]. Since this type of directional acoustic sensor measures both the *scalar* acoustic pressure and the x, y and z components of the *vector* part of the acoustic wave field (e.g., the acoustic particle displacement, velocity or acceleration), it has been called an *acoustic vector sensor* [4,5,6]. A single acoustic vector sensor can provide up to 6 dB of array gain against isotropic noise relative to an acoustic scalar sensor or omnidirectional hydrophone [5]. This vector sensor can also unambiguously estimate the direction of arrival (DOA) of an acoustic source [4]. Further, this vector sensor can produce a frequency-independent beam pattern with a 3-dB beamwidth of 105 degrees [6,7]. If three accelerometers and a pressure sensor (i.e., a vector sensor) can achieve the above results, a question that naturally follows is how many more individual sensors (e.g., accelerometers and/or pressure sensors) must fit into a given sensor housing or form factor to improve upon the aforementioned directionality of the acoustic vector sensor? In Section 2.0, formulating a rigorous mathematical framework for the general theory of directional acoustic sensors provides a partial answer. From this theory we show that the next logical step to further improve vector sensor directionality is to define the *acoustic dyadic sensor*. Section 3 shows that, for a general linear acoustic wave, 19 judiciously placed pressure sensors or 18 accelerometers and one pressure sensor can approximate the acoustic dyadic sensor. Section 4 consists of an acoustic analysis of a theoretical dyadic sensor, and Section 5 shows how an acoustic dyadic sensor can be used to create a Multichannel filter. Experimental results from a Seneca Lake test, conducted in May 2001, are presented in Section 6.0. Measured beam patterns for a partial dyadic sensor, implemented by six accelerometers and a pressure sensor, are presented in Section 6.1. In Section 6.2, we show how multi-channel signal processing of a vector sensor can be used to realize the performance of a dyadic sensor when the pressure field is assumed to be an arbitrary plane wave. We also provide experimental results to validate this claim. We close this report with Section 7.0, which provides a summary and recommendations for future research.

## 2.0 General Theory of Directional Acoustic Sensors

Let us consider a single acoustic sensor located at some measurement point  $\vec{r}_0 = (x_0, y_0, z_0)$ . A Taylor series for the scalar acoustic pressure field  $p(t, \vec{r})$  about this point would include the scalar (tensor of order zero) pressure  $p(t, \vec{r}_0)$  as the zero-order term, the pressure gradient/vector (tensor of order one)  $\nabla p(t, \vec{r}_0)$  at the point as part of the first-order term, the dyadic (tensor of order two)  $\nabla \nabla p(t, \vec{r}_0)$  at the point as part of the

second order term, and so on. Using this Taylor series, we define a general class of directional acoustic sensors as follows [6]. A **scalar acoustic pressure sensor** (e.g., a hydrophone) will be referred to as a directional acoustic sensor of order zero. This sensor only measures the scalar acoustic pressure  $p(t, \vec{r}_0)$  at the point  $\vec{r}_0$ ; its Taylor series about  $\vec{r}_0$  assumes that the acoustic pressure field  $p(t, \vec{r})$  about that point is independent of the field point  $\vec{r} = (x, y, z)$ . An **acoustic vector sensor** will be referred to as a directional acoustic sensor of order one. This sensor measures both  $p(t, \vec{r}_0)$  and the pressure gradient/vector  $\nabla p(t, \vec{r}_0)$  at the point  $\vec{r}_0$ ; its Taylor series about  $\vec{r}_0$  assumes that the acoustic pressure field  $p(t, \vec{r})$  about that point is a linear function of the field point  $\vec{r}$ . Similarly, an **acoustic dyadic sensor** will be referred to as a directional acoustic sensor of order two. This sensor measures  $p(t, \vec{r}_0)$ ,  $\nabla p(t, \vec{r}_0)$  and the dyadic  $\nabla \nabla p(t, \vec{r}_0)$  at the point  $\vec{r}_0$ ; its Taylor series about  $\vec{r}_0$  assumes that the acoustic pressure field  $p(t, \vec{r})$  about that point is a quadratic function of the field point  $\vec{r}$ .

D'Spain [8] was the first to point out a qualitative relationship between the Taylor series expansion of the pressure field and a vector sensor. Following his observation, we consider a single acoustic sensor located at some measurement point  $\vec{r}_0 = (x_0, y_0, z_0)$ . The Taylor series for the pressure  $p(x, y, z, t)$  expanded about the point  $(x_0, y_0, z_0)$  is

$$p(x, y, z, t) = p(x_0, y_0, z_0, t) + \left[ (x - x_0) \frac{\partial}{\partial x} + (y - y_0) \frac{\partial}{\partial y} + (z - z_0) \frac{\partial}{\partial z} \right] p(x_0, y_0, z_0, t) + \frac{1}{2} \left[ (x - x_0) \frac{\partial}{\partial x} + (y - y_0) \frac{\partial}{\partial y} + (z - z_0) \frac{\partial}{\partial z} \right]^2 p(x_0, y_0, z_0, t) + R_3 \quad (1)$$

where  $p(x_0, y_0, z_0, t)$  following the brackets means that the partials within the brackets are to operate upon  $p$  at the point  $(x_0, y_0, z_0)$ , and the brackets indicate that the expansion of the quantity within is to be a trinomial expansion except that

$$\left( \frac{\partial}{\partial x} \right)^n \left( \frac{\partial}{\partial y} \right)^k \quad (2)$$

is to be replaced by

$$\frac{\partial^{n+k}}{\partial x^n \partial y^k} \quad (3)$$

and terms like

$$\left( \frac{\partial}{\partial x} \right)^0 \quad (4)$$

are to be replaced by 1. Let us define the column vectors

$$\underline{r} = \begin{bmatrix} x \\ y \\ z \end{bmatrix}, \underline{r}_0 = \begin{bmatrix} x_0 \\ y_0 \\ z_0 \end{bmatrix} \quad (5)$$

$$\nabla p(x_0, y_0, z_0, t) \equiv \left[ \frac{\partial p}{\partial x} \quad \frac{\partial p}{\partial y} \quad \frac{\partial p}{\partial z} \right]' \bigg|_{x=x_0, y=y_0, z=z_0} \quad (6)$$

and the Hessian matrix

$$\nabla \nabla p(x_0, y_0, z_0, t) \equiv \begin{bmatrix} \frac{\partial^2 p}{\partial x^2} & \frac{\partial^2 p}{\partial x \partial y} & \frac{\partial^2 p}{\partial x \partial z} \\ \frac{\partial^2 p}{\partial y \partial x} & \frac{\partial^2 p}{\partial y^2} & \frac{\partial^2 p}{\partial y \partial z} \\ \frac{\partial^2 p}{\partial z \partial x} & \frac{\partial^2 p}{\partial z \partial y} & \frac{\partial^2 p}{\partial z^2} \end{bmatrix} \bigg|_{x=x_0, y=y_0, z=z_0} \quad (7)$$

Using (5) through (7) in (1) and dropping the remainder term  $R_3$ , we obtain

$$\begin{aligned} \hat{p}(x, y, z, t) = & p(x_0, y_0, z_0, t) + (\underline{r} - \underline{r}_0) \nabla p(x_0, y_0, z_0, t) \\ & + \frac{1}{2} (\underline{r} - \underline{r}_0) \nabla \nabla p(x_0, y_0, z_0, t) (\underline{r} - \underline{r}_0) \end{aligned} \quad (8)$$

The function  $\hat{p}(x, y, z, t)$  is the pressure estimate generated by the dyadic sensor and is capable of extrapolating the acoustic pressure field beyond the measurement point  $\vec{r}_0$  so that it actually knows this field at every point inside a sphere of radius  $R = |\vec{r} - \vec{r}_0|$ , where  $R$  is defined by the type of directional sensor and the error associated with the extrapolation. The Taylor series (8) is the formula used to do the wave field extrapolation with some specified error  $\varepsilon(t, \vec{r})$ . For example, a directional sensor of order zero, can only measure the pressure at  $\vec{r}_0$ , so its estimate of the field beyond this point is  $\hat{p}(t, \vec{r}) = p(t, \vec{r}_0)$  and the corresponding estimation or extrapolation error is  $\varepsilon(t, \vec{r}) \equiv p(t, \vec{r}) - p(t, \vec{r}_0)$ . If the error is required to be small (less than 10%), then  $R$  will be small. This implies that the aperture ( $2R$ ) of a single pressure sensor is small, so by the theory of spatial Fourier transforms [9], the zero-order sensor is essentially omnidirectional. However, a sensor of order one (vector sensor) measures both the pressure and pressure gradient at  $\vec{r}_0$ , so its estimate of the field beyond this point is  $\hat{p}(t, \vec{r}) = p(t, \vec{r}_0) + (\vec{r} - \vec{r}_0) \cdot \nabla p(t, \vec{r}_0)$  and the corresponding estimation error is

$$\begin{aligned}\varepsilon(t, \vec{r}) &\equiv p(t, \vec{r}) - \hat{p}(t, \vec{r}) \\ \varepsilon(t, \vec{r}) &= p(t, \vec{r}) - [p(t, \vec{r}_0) + (\vec{r} - \vec{r}_0) \cdot \nabla p(t, \vec{r}_0)]\end{aligned}\quad (9)$$

For the same error, the vector sensor will have a larger aperture than the scalar sensor, so it should be more directional. Thus, the dyadic sensor should be better than the scalar and vector sensors at estimating the field, so it should be even more directional.

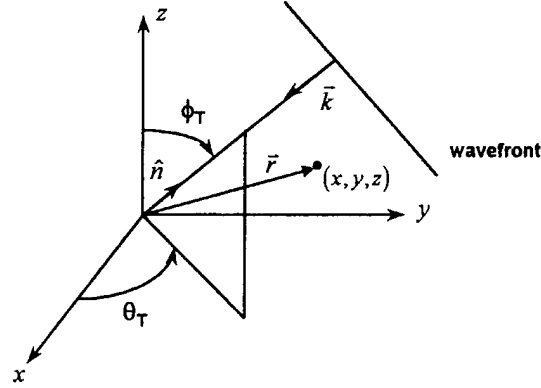


Figure 1. The propagation of a planar wavefront toward the origin of a rectangular coordinate system.

For the case of a plane wave pressure field (refer to Figure 1), we define the mean-squared error in estimating the pressure field beyond  $\vec{r}_0$  by

$$MSE = \frac{1}{\pi T} \int_0^{\pi} \int_0^{\pi} |\varepsilon(t, \vec{r})|^2 dt d\beta, \quad (10)$$

where  $T$  is a suitable integration time (e.g., the temporal period of a plane wave) and  $\beta$  is the angle between  $\hat{n}$  and  $\hat{r}$  (a unit vector in the direction of  $\vec{r}$ ).

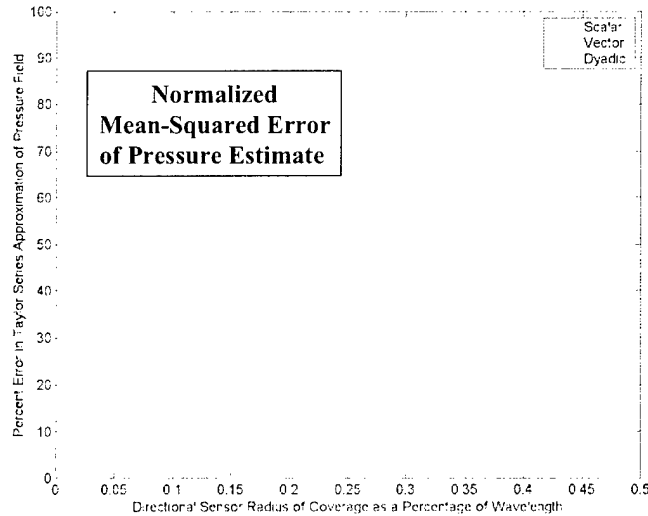


Figure 2. Normalized mean-squared estimation error (equation (19)) vs.  $R/\lambda$ .

Dividing (10) by the average power in the acoustic pressure field we obtain the normalized MSE. Figure 2 shows the normalized mean-squared error as a function of  $R/\lambda$  for the scalar, vector and dyadic sensors. For a specified normalized MSE of 10%, notice that the acoustic aperture ( $2R$ ) of the scalar sensor is about  $\lambda/10$ , whereas the apertures for the vector and dyadic sensors are  $\lambda/3$  and  $\lambda/2$ , respectively. Figure 3 is scaled to graphically depict the situation.

#### Taylor Series Extrapolation of Pressure Field = Volumetric Spherical Sensors

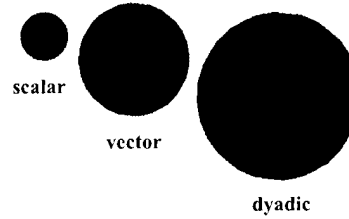


Figure 3. Spherical coverage for 10% error.

We are now in the position to answer the question posed in the Introduction: *If three accelerometers and a pressure sensor (i.e., a vector sensor) can achieve the above results, a question that naturally follows is how many more individual sensors (e.g., accelerometers and/or pressure sensors) must fit into a given sensor housing or form factor to improve upon the aforementioned directionality of the acoustic vector sensor?* Recall that the dyadic sensor measures  $p(t, \vec{r}_0)$ ,  $\nabla p(t, \vec{r}_0)$  and the dyadic  $\nabla \nabla p(t, \vec{r}_0)$  at the point  $\vec{r}_0$ . According to (6), (7), and (8), we must measure 13 terms involving the pressure and the first and second partial derivatives of the pressure. Due to the symmetry of the mixed partials in (7), the number of distinct terms reduces to 10. The next section demonstrates that these 10 terms can be estimated by 19 judiciously spaced pressure sensors, or 18 judiciously spaced accelerometers and 1 pressure sensor placed at the origin.

### 3.0 Realization of an Acoustic Dyadic Sensor

The goal of this section is to show how finite difference approximations can be used to estimate the 10 terms that define the dyadic sensor; that is, the scalar pressure, the 3 terms of the pressure gradient, and the 6 distinct terms in the Hessian matrix. We will first show how to realize the dyadic sensor by using 19 pressure sensors, then we will provide a dyadic sensor realization that uses 18 judiciously spaced accelerometers and one pressure sensor at the origin. Both realizations utilize a symmetrical placement of

sensors, which allows us to consider the sensors as collocated with a common phase center at the origin.

### 3.1 Finite-Difference Approximation of the Pressure Gradient

Figure 4 illustrates an arrangement of pressure sensors useful for estimating the first partial derivatives  $\frac{\partial p}{\partial x}$ ,  $\frac{\partial p}{\partial y}$  and  $\frac{\partial p}{\partial z}$  at  $(0,0,0)$ . The finite-difference approximations of the pressure gradient are given by

$$\frac{\partial p(t,0,0,0)}{\partial x} \approx [p(t,h,0,0) - p(t,-h,0,0)]/2h \quad (11a)$$

$$\frac{\partial p(t,0,0,0)}{\partial y} \approx [p(t,0,h,0) - p(t,0,-h,0)]/2h \quad (11b)$$

$$\frac{\partial p(t,0,0,0)}{\partial z} \approx [p(t,0,0,h) - p(t,0,0,-h)]/2h \quad (11c)$$

The errors of the above approximations are on the order of  $h^2$ . Note that 6 pressure sensors are required to realize the pressure gradient.

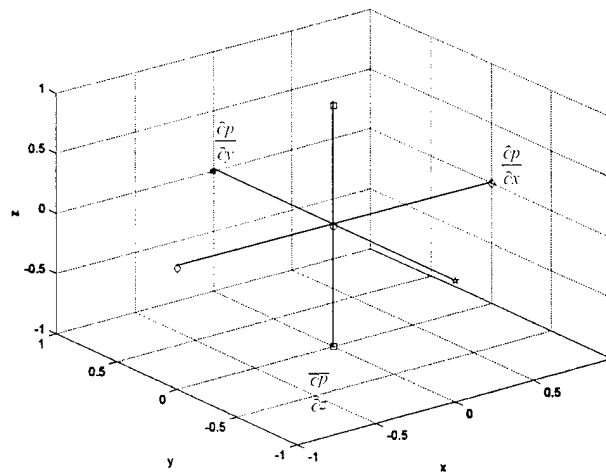


Figure 4. The arrangement of six pressure sensors for the finite-difference approximation of the pressure gradient.

### 3.2 Finite-Difference Approximation of the Hessian of the Pressure

Figure 5 illustrates an arrangement of pressure sensors useful for estimating the second partial derivatives  $\frac{\partial^2 p}{\partial x^2}$ ,  $\frac{\partial^2 p}{\partial y^2}$  and  $\frac{\partial^2 p}{\partial z^2}$  at  $(0,0,0)$ . The finite-difference approximations of these partials are given by

$$\frac{\partial^2 p(0,0,0,t)}{\partial x^2} \approx \frac{p(h,0,0,t) - 2p(0,0,0,t) + p(-h,0,0,t)}{h^2} \quad (12a)$$

$$\frac{\partial^2 p(0,0,0,t)}{\partial y^2} \approx \frac{p(0,h,0,t) - 2p(0,0,0,t) + p(0,-h,0,t)}{h^2} \quad (12b)$$

$$\frac{\partial^2 p(0,0,0,t)}{\partial z^2} \approx \frac{p(0,0,h,t) - 2p(0,0,0,t) + p(0,0,-h,t)}{h^2} \quad (12c)$$

The errors of the above approximations are on the order of  $h^2$ . Note from (12) and from Figure 5 that there are 7 pressure sensors involved in the estimation of  $\frac{\partial^2 p}{\partial x^2}$ ,  $\frac{\partial^2 p}{\partial y^2}$  and  $\frac{\partial^2 p}{\partial z^2}$  at  $(0,0,0)$ . The pressure sensor at the origin is also utilized to measure the acoustic pressure at  $(0,0,0)$ . This pressure is the first term in the pressure estimate given by (8) where  $x_0 = y_0 = z_0 = 0$ . The other six sensors in Figure 5 are the same sensors that provide data for the estimates appearing in Equations (11).

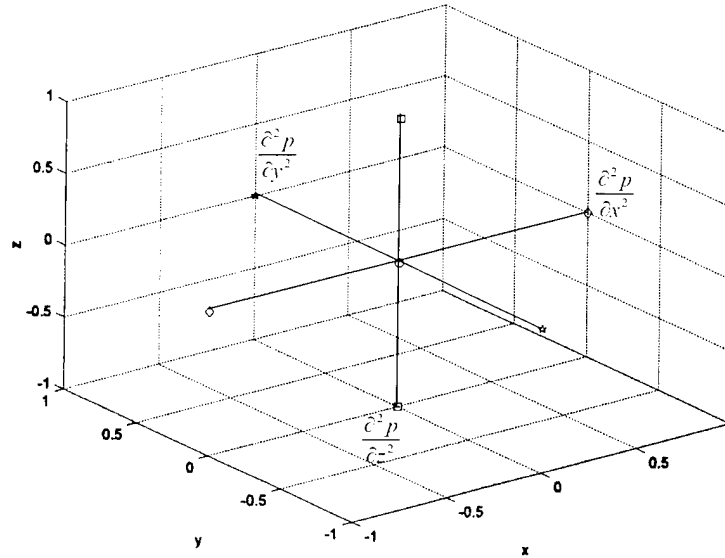


Figure 5. Sensor placement for the estimation of the diagonal elements of the Hessian of the pressure at the origin.



Figure 6 illustrates an arrangement of pressure sensors useful for estimating the mixed second partial derivatives  $\frac{\partial^2 p}{\partial x \partial y}$ ,  $\frac{\partial^2 p}{\partial x \partial z}$  and  $\frac{\partial^2 p}{\partial y \partial z}$  at  $(0,0,0)$ . The four “star” sensors can be used to estimate  $\frac{\partial^2 p}{\partial x \partial y} \Big|_{x=y=z=0}$ , the four “diamond” sensors can be used to estimate  $\frac{\partial^2 p}{\partial x \partial z} \Big|_{x=y=z=0}$ , and the four “square” sensors can be used to estimate  $\frac{\partial^2 p}{\partial y \partial z} \Big|_{x=y=z=0}$ . The finite-difference approximations of these partials are given by

$$\frac{\partial^2 p(0,0,0,t)}{\partial x \partial y} \approx \frac{p(\frac{h}{2}, \frac{h}{2}, 0, t) - p(\frac{h}{2}, -\frac{h}{2}, 0, t) - p(-\frac{h}{2}, \frac{h}{2}, 0, t) + p(-\frac{h}{2}, -\frac{h}{2}, 0, t)}{h^2} \quad (13a)$$

$$\frac{\partial^2 p(0,0,0,t)}{\partial x \partial z} \approx \frac{p(\frac{h}{2}, 0, \frac{h}{2}, t) - p(\frac{h}{2}, 0, -\frac{h}{2}, t) - p(-\frac{h}{2}, 0, \frac{h}{2}, t) + p(-\frac{h}{2}, 0, -\frac{h}{2}, t)}{h^2} \quad (13b)$$

$$\frac{\partial^2 p(0,0,0,t)}{\partial y \partial z} \approx \frac{p(0, \frac{h}{2}, \frac{h}{2}, t) - p(0, \frac{h}{2}, -\frac{h}{2}, t) - p(0, -\frac{h}{2}, \frac{h}{2}, t) + p(0, -\frac{h}{2}, -\frac{h}{2}, t)}{h^2} \quad (13c)$$

The errors of the above approximations are on the order of  $h^2$ . Note from (13) and from Figure 6 that there are a total of 12 pressure sensors involved in the estimation of  $\frac{\partial^2 p}{\partial x \partial y}$ ,  $\frac{\partial^2 p}{\partial x \partial z}$  and  $\frac{\partial^2 p}{\partial y \partial z}$  at  $(0,0,0)$ . This makes a total of 19 sensors: 7 for the estimation of the gradient and the diagonal terms of the Hessian and 12 for the estimation of the off-diagonal terms of the Hessian.

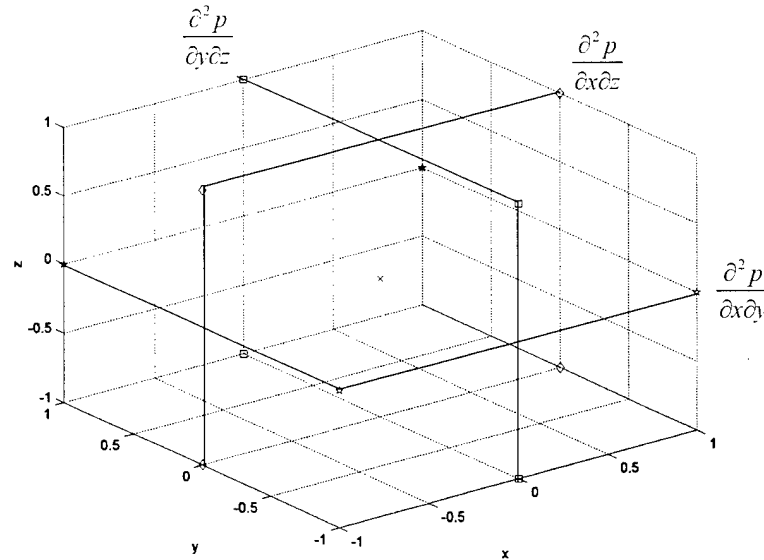


Figure 6. Sensor placement for the estimation of the off-diagonal elements of the Hessian of the pressure at the origin.

### 3.3 Realization of a Dyadic Sensor by Means of Accelerometers

From Newton's Second Law of Motion, the pressure gradient and acoustic particle acceleration vector are related by

$$\nabla p = -\rho \vec{a} \quad (14)$$

Taking the vector gradient of both sides of (14) results in the dyadic/Hessian

$$\nabla \nabla p = -\nabla(\rho \vec{a}) = -\rho \nabla \vec{a} - \vec{a} \nabla \rho \approx -\rho \nabla \vec{a} \quad (15)$$

where

$$\nabla \vec{a} \equiv \begin{bmatrix} \frac{\partial a_x}{\partial x} & \frac{\partial a_x}{\partial y} & \frac{\partial a_x}{\partial z} \\ \frac{\partial a_y}{\partial x} & \frac{\partial a_y}{\partial y} & \frac{\partial a_y}{\partial z} \\ \frac{\partial a_z}{\partial x} & \frac{\partial a_z}{\partial y} & \frac{\partial a_z}{\partial z} \end{bmatrix} \quad (16)$$

is the gradient of  $\vec{a}$ ,  $\rho$  is the mass density and  $\nabla \rho$  is the gradient of the mass density at the origin. Note the approximation appearing in (15). According to Camp [10], a reasonable acoustic approximation is to neglect  $\nabla \rho$  at the origin. Equations (14) and (15) are two of the three quantities measured by a dyadic sensor (pressure being the third one). First-order finite difference approximations can be used to estimate the elements of (16). This would require 18 accelerometers symmetrically arranged as in Figures 5 and 6. Like the pressure sensor realization of the dyadic sensor, the accelerometer realization utilizes a symmetrical placement of accelerometers, which allows us to consider the accelerometers as collocated with a common phase center at the origin.

### 3.4 Comparison of Pressure and Accelerometer Realizations of the Dyadic Sensor

Table 1 provides comparisons between the pressure and acceleration methods of dyadic sensor realization:

**Table 1**

<b>Pressure Realization</b>	<b>Accelerometer Realization</b>
Requires 19 pressure sensors with one at the origin. See Figures 5 and 6 for placement.	Requires 19 sensors (18 accelerometers and one pressure sensor). See Figures 5 and 6 for placement.
One hydrophone at origin measures pressure	One hydrophone at origin measures pressure
Estimates the pressure gradient by first-order finite differences.	Measures the pressure gradient. See Eq. (14).
Does not require knowledge of $\rho$ at the measurement point to estimate the Hessian.	Requires knowledge of $\rho$ at the measurement point to estimate the Hessian.
Requires first-order and second-order finite-difference approximations	Requires only first-order finite-difference approximations

## 4.0 Analysis of a Theoretical Acoustic Dyadic Sensor

This section will examine the effects of finite-difference approximations on the estimation of the pressure gradient and Hessian (realization by pressure sensors). It will also examine the effects of finite-difference approximations on the estimation of  $\nabla \vec{a}$  (realization by accelerometers).

### 4.1 Pressure Gradient Estimation

In the underwater and in-air communities, the pressure gradient/vector, needed for a vector sensor, is found in a variety of different ways. As discussed above, one can measure the acoustic particle acceleration vector  $\vec{a}(t, \vec{r}_0)$  directly and use (14) and knowledge of the mass density at the measurement point  $\vec{r}_0$  to obtain a fairly accurate value of the pressure gradient  $\nabla p(t, \vec{r}_0)$ . Alternatively, one could measure the acoustic particle velocity vector  $\vec{v}(t, \vec{r}_0)$  directly, perform a time derivative to get the acceleration vector and proceed as above to get the pressure gradient. (The accuracy of this method would depend on how well one implemented the time derivative). If one decides to use scalar pressure sensors to approximate the pressure gradient, then the finite difference approximations in (11) would have to be computed. However, great care must be exercised when approximating the pressure gradient by (11). For example, (11a) approximates the x-component of the pressure gradient at the measurement point  $\vec{r}_0 = (0,0,0)$ . (Refer to Figure 4). If the pressure field was the arbitrary (narrowband or broadband) plane wave

$$p(t, \vec{r}) = f\left(t + \frac{\hat{n} \cdot \vec{r}}{c}\right), \quad (17)$$

which is assumed to be propagating toward the origin of the coordinate system in Figure 1, then the exact value of the temporal Fourier transform of the pressure gradient would be

$$\nabla P(\omega, \vec{r}) = jF(\omega) \vec{k} e^{j\vec{k} \cdot \vec{r}} = jP(\omega, \vec{r}) \vec{k}. \quad (18)$$

Here, the wavenumber or propagation vector  $\vec{k} = k\hat{n}$  has the magnitude  $k = \omega/c = 2\pi/\lambda$  and the direction  $\hat{n}$ , where  $\hat{n}$  is the unit vector

$$\hat{n} = \sin \phi_T \cos \theta_T \hat{x} + \sin \phi_T \sin \theta_T \hat{y} + \cos \phi_T \hat{z}. \quad (19)$$

The position vector

$$\vec{r} = x\hat{x} + y\hat{y} + z\hat{z} = r \sin \phi \cos \theta \hat{x} + r \sin \phi \sin \theta \hat{y} + r \cos \phi \hat{z} \quad (20)$$

is the vector from the origin to an arbitrary field point  $\vec{r} = (x, y, z)$  in rectangular coordinates or  $\vec{r} = (r \sin \phi \cos \theta, r \sin \phi \sin \theta, r \cos \phi)$  in spherical coordinates. The temporal Fourier transform of the plane wave pressure field (17) is found by using

$$P(\omega, \vec{r}) = \int_{-\infty}^{\infty} p(t, \vec{r}) e^{-j\omega t} dt. \quad (21)$$

Now if we use (11a) to approximate the x-component of the pressure gradient at the origin (the point  $\vec{r}_0 = (0, 0, 0)$ ), then the temporal Fourier transform of this approximation can be expressed as

$$\frac{\partial P(\omega, \vec{r}_0)}{\partial x} = P_x(\omega, \vec{r}_0) \approx \hat{P}_x(\omega, \vec{r}_0) = jF(\omega) \frac{\sin(k_x h)}{h}. \quad (22)$$

Since the exact value of  $P_x(\omega, \vec{r}_0)$  is given by

$$P_x(\omega, \vec{r}_0) = jk_x F(\omega), \quad (23)$$

as  $h \rightarrow 0$ , the estimate given by (22) approaches the exact value given by (23). A good measure of the quality of the gradient estimation is the decibel error  $\mathcal{E}$ , namely,

$$\mathcal{E} = 20 \log \left| \frac{\hat{P}_x}{P_x} \right| \quad (24)$$

Since  $h = \Delta x/2$ , where  $\Delta x$  is the sensor spacing, we have from (22) and (23) that

$$\mathcal{E} = 20 \log |\text{sinc}(k_x \Delta x/2)| \quad (25)$$

Figure 7 illustrates the error  $\mathcal{E}$  as a function of  $\Delta x/\lambda$  for the case  $\phi_r = 90^\circ$  and  $\theta_r = 0^\circ$ . An error of  $-0.5$  dB will occur for a spacing of  $\Delta x = 0.186\lambda$  or  $0.186$  wavelengths. A spacing of one-tenth of a wavelength will yield an error of  $-0.14$  dB. Another popular measure of the quality of estimation is the percent error defined as

$$\delta_e = \left( \left| \frac{\hat{P}_x}{P_x} \right| - 1 \right) \times 100 \quad (26)$$

The relationship between  $\delta_e$  and  $\mathcal{E}$  is illustrated in Figure 8. For example, a value for  $\mathcal{E}$  of  $0.4$  dB corresponds to a  $\delta_e$  of about  $4.7\%$ .

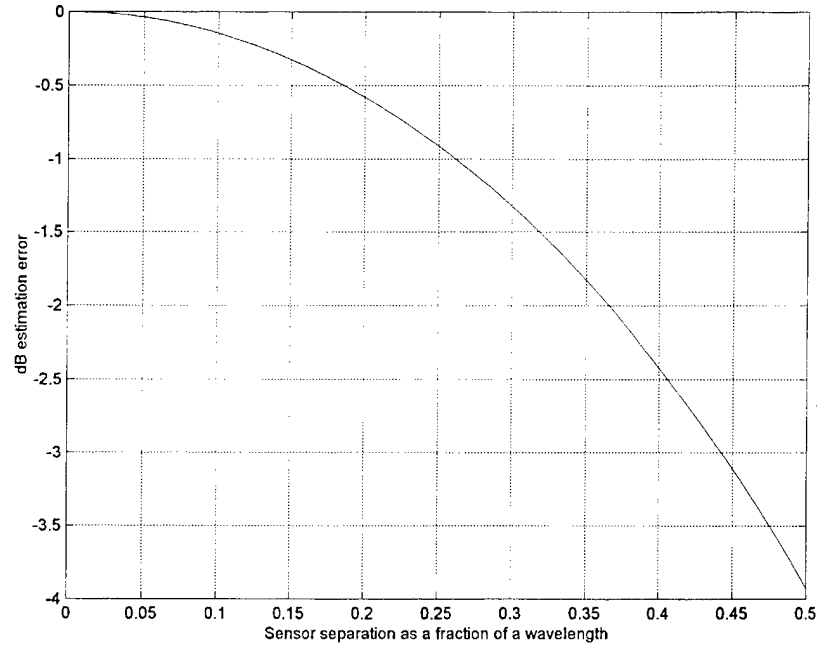


Figure 7. The error  $\epsilon$  in estimating the partial derivative of the pressure with respect to  $x$  (at the origin).  $\phi_T = 90^\circ$  and  $\theta_T = 0^\circ$ .

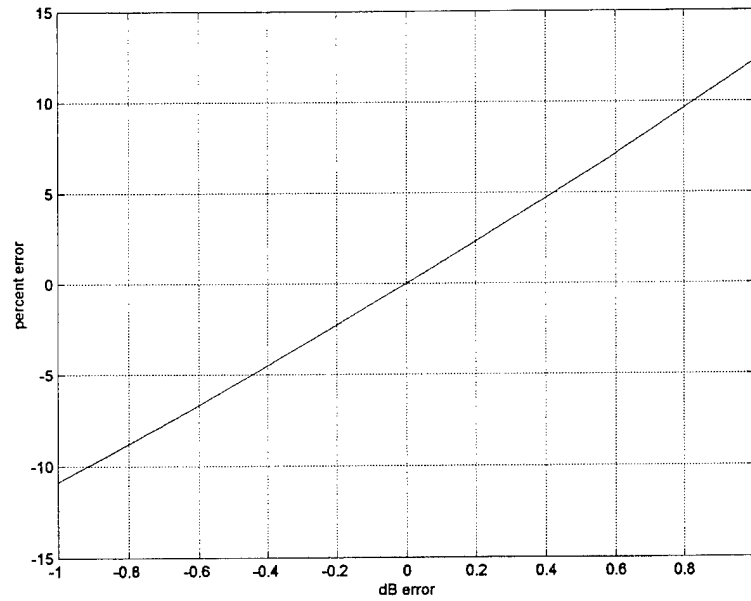


Figure 8. Relationship between percent error and dB error.

Notice that (25) is frequency dependent because of the presence of  $k_x$  and is valid only when the two hydrophones in the  $x$ -axis dipole (Refer to Figure 4) are exactly matched in

their amplitude and phase frequency responses. In practice, this is seldom the case, so we must modify our analysis to include the effects of mismatch in the frequency responses of the hydrophone and corresponding signal conditioning associated with each hydrophone in the dipole. The temporal Fourier transform of (17) is

$$P(\omega, \vec{r}) = F(\omega) e^{jk \cdot \vec{r}} \quad (27)$$

However, when the pressure waveform impinges on the sensor, the sensor would transform this pressure to the analog voltage Fourier transform

$$V(\omega, \vec{r}) = K(\omega) P(\omega, \vec{r}) \quad (28)$$

The quantity  $K(\omega)$  is the composite (sensor sensitivity plus electronics) frequency response of the sensor. Taking the temporal Fourier transform of (11a) and incorporating the composite frequency responses of the two sensors, we arrive at

$$V(\omega, \vec{r}_0) = F(\omega) \frac{K_1(\omega) e^{jk_x h} - K_2(\omega) e^{-jk_x h}}{2h} \quad (29)$$

Let the mismatch between the two sensors be described by the quantity

$$M(\omega) = \frac{K_2(\omega)}{K_1(\omega)} = \mu(\omega) \exp[j\zeta(\omega)], \quad (30)$$

where  $\mu(\omega)$  and  $\zeta(\omega)$  are the amplitude and phase mismatch, respectively.

Utilizing (30) in (29) gives

$$\frac{V(\omega, \vec{r}_0)}{K_1(\omega)} = F(\omega) \frac{e^{jk_x h} - \mu(\omega) e^{j[-k_x h + \zeta(\omega)]}}{2h} \quad (31)$$

The magnitude of (31) is

$$\left| \frac{V(\omega, \vec{r}_0)}{K_1(\omega)} \right| = \left| \hat{P}_x(\omega, \vec{r}_0) \right| = |F(\omega)| \frac{\sqrt{1 - 2\mu \cos(2k_x h - \zeta) + \mu^2}}{2h} \quad (32)$$

The dB gradient estimation error has the value

$$\epsilon = 20 \log \left| \frac{\sqrt{1 - 2\mu \cos(2k_x h - \zeta) + \mu^2}}{2k_x h} \right| \quad (33)$$

When  $\mu = 1$  and  $\zeta = 0$ , there is no amplitude and phase mismatch and (33) reduces to (25). The error  $\mathcal{E}$  becomes infinite when  $k_x = 0$ . However,  $k_x = 0$  means that the pressure waveform is not a function of  $x$ , and we would not be estimating the partial derivative of the pressure with respect to  $x$  since it is zero. From Equation (11a) we observe that the separation between the two sensors along the  $x$  axis is  $\Delta x = 2h$ . Assuming that  $\zeta = 0$  (no phase mismatch) and noting that  $k_x = 2\pi n_x / \lambda$ , we can write (33) as

$$\mathcal{E} = 20 \log \left| \frac{\sqrt{1 - 2\mu \cos(2\pi(n_x \Delta x / \lambda)) + \mu^2}}{2\pi(n_x \Delta x / \lambda)} \right| \quad (34)$$

Figure 9 is a contour plot of  $\mathcal{E}$  versus  $\Delta x / \lambda$  and  $\mu$  for the case  $n_x = \sin \phi_T \cos \theta_T = \pm 1$  ( $\mathcal{E}$  is an even function of  $n_x$ ). The contours shown correspond to  $\mathcal{E} = \pm 1, \pm 0.5$  and 0

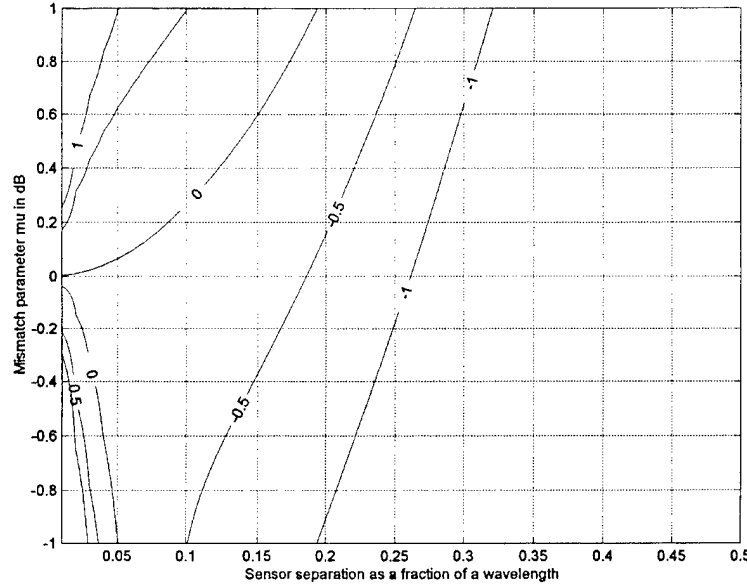


Figure 9. Contour plot of the error  $\mathcal{E}$  as a function of  $\mu$  and  $\Delta x / \lambda$  for the case  $n_x = \pm 1$ .

dB. From the figure we see that to achieve a gradient estimation error of  $-0.5$  dB ( $-5.6\%$ ) when the sensor amplitude mismatch is  $\mu = -1$  dB, we need a sensor spacing of  $0.1$  wavelengths. This is  $46\%$  smaller than the required relative spacing with no mismatch. Figure 10 is a contour plot for the case  $n_x = \pm \frac{1}{2}$ . Note that for the same  $\mathcal{E}$  and  $\mu$  the sensor spacing is now  $0.2$  wavelengths or double the previous value. For an arbitrary  $n_x$ , the new spacing would be  $0.1/|n_x|$  wavelengths. Note that the spacing increases as  $|n_x|$  decreases. Hence,  $|n_x| = 1$  is the most restrictive case and Figure 9 should be used to determine the required sensor spacing.

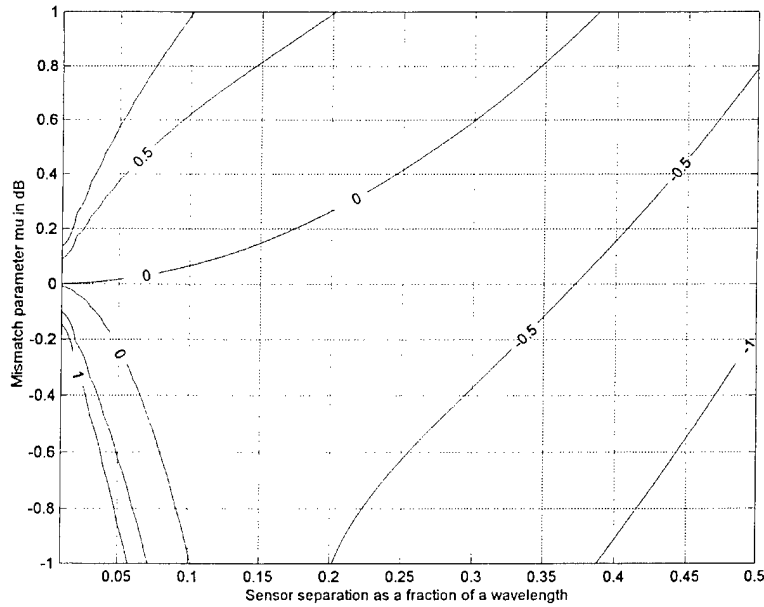


Figure 10. A contour plot of the error  $\epsilon$  for the case  $n_x = \pm \frac{1}{2}$ .

#### 4.2 Estimation of the Pure Second-Order Partial Derivatives of Pressure

This section performs an analysis of the error that results in utilizing finite-difference approximations to estimate the pure second-order derivatives of acoustic pressure. The

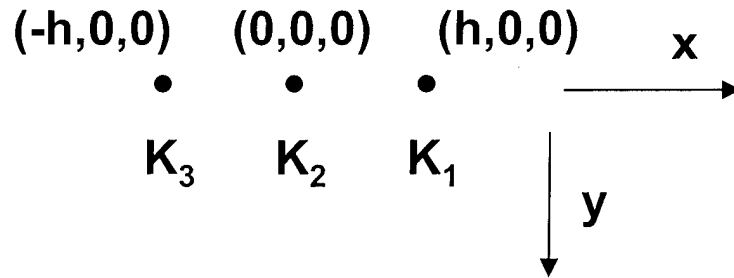


Figure 11. Arrangement of pressure sensors for the finite-difference approximation of the pure second-order partial  $\partial^2 p / \partial x^2$  at the origin.

errors that will be considered are those due to non-zero sensor spacing and to mismatch in the frequency responses of the various sensors. We will be concerned with the second-order partial derivative  $\partial^2 p(0,0,0,t) / \partial x^2$ . The results of error analyses of the two other pure second-order partial derivatives would be analogous. Figure 11 shows the arrangement of the pressure sensors. Starting with the estimation equation (13a) we would arrive at an equation analogous to (29), namely,



$$V_{xx}(\omega) = F(\omega) \frac{K_1 \exp(jk_x h) - 2K_2 + K_3 \exp(-jk_x h)}{h^2} \quad (35)$$

If  $K_3 = K_2 = K_1$  (no mismatch), then (35) reduces to

$$V_{xx}(\omega) = -k_x^2 K_1 F(\omega) \text{sinc}^2(k_x h/2) \quad (36)$$

From Figure 5 we observe that the relative sensor spacing is  $\Delta x = h$ . The error  $\mathcal{E}$  is given by

$$\mathcal{E} = 20 \log \left| \frac{\partial^2 \hat{P}(\bar{0}, \omega)}{\partial x \partial y} \right| = 20 \log \left| \frac{\hat{P}_{xx}}{P_{xx}} \right| = 40 \log |\text{sinc}(k_x \Delta x/2)| \quad (37)$$

Equation (37) approaches zero as  $\Delta x$  approaches zero. A comparison of (37) with (25) reveals that for a given sensor separation  $\Delta x$ , the error in estimating the pure second-order partial derivative is twice the error in estimating the first-order partial derivative. The problem is more complicated when the sensors are mismatched. The magnitude of (35) has the form

$$|V_{xx}(\omega)| = K_1 \frac{|F(\omega)|}{h^2} \sqrt{\underline{\mu}' \Gamma \underline{\mu}} \quad (38)$$

where

$$\underline{\mu} = \begin{bmatrix} 1 \\ K_2/K_1 \\ K_3/K_1 \end{bmatrix} = \begin{bmatrix} 1 \\ \mu_2 \\ \mu_3 \end{bmatrix} \quad (39)$$

$$\Gamma = \begin{bmatrix} 1 & -2 \cos(k_x h) & \cos(2k_x h) \\ -2 \cos(k_x h) & 4 & -2 \cos(k_x h) \\ \cos(2k_x h) & -2 \cos(k_x h) & 1 \end{bmatrix} \quad (40)$$

For this more general case, (37) becomes

$$\mathcal{E} = 20 \log \left| \frac{\sqrt{\underline{\mu}' \Gamma \underline{\mu}}}{(k_x \Delta x)^2} \right| \quad (41)$$

If each element in  $\underline{\mu}$  is one, then (41) reduces to (37). In the current error analysis we have ignored the mismatch in phase response between sensors. A more complete analysis would result in addition of a phase terms in the arguments of the cosines that appear in (40). To see the effect of sensor mismatch on the dB error  $\mathcal{E}$ , let us begin by computing the relative sensor spacing to achieve an  $\mathcal{E}$  of  $-0.4$  dB (4.7% error) when

$\phi_T = 90^\circ$  and  $\theta_T = 0^\circ$ . If we use (37) we will obtain  $\Delta x/\lambda = 0.118$ . Figure 12 shows a contour plot of  $\epsilon$  in dB versus the mismatch parameters  $\mu_2$  and  $\mu_3$  for the special case  $\phi_T = 90^\circ$ ,  $\theta_T = 0^\circ$  and  $\Delta x/\lambda = 0.118$ . Observe from Figure 12 that when  $\mu_3 = \mu_2 = 0$  dB, the value of  $\epsilon$  is  $-0.4$  dB as expected. We see from the figure, that sensor mismatch may improve the error (note the 0 dB error contour). However, the error can get much larger. For example, if  $\mu_2 = -0.5$  and  $\mu_3 = +0.5$  dB, the value of  $\epsilon$  increases to about 2 dB.

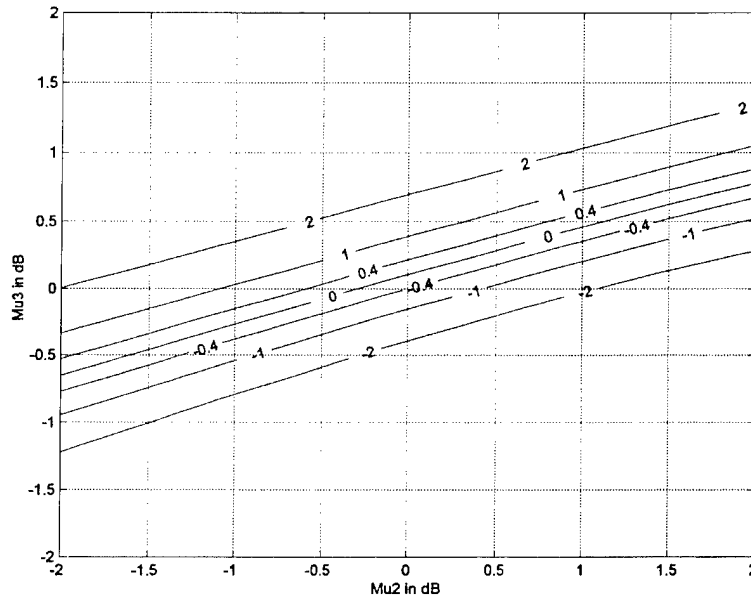


Figure 12. Contour plot for  $\epsilon$  as a function of the mismatch parameters  $\mu_2$  and  $\mu_3$  for the special case of  $\phi_T = 90^\circ$ ,  $\theta_T = 0^\circ$  and  $\Delta x/\lambda = 0.118$ .

### 4.3 Estimation of the Mixed Second-Order Partial Derivatives of Pressure

This section performs an analysis of the error that results in utilizing finite-difference approximations to estimate the mixed second-order derivatives of acoustic pressure. The errors that will be considered are those due to non-zero sensor spacing and to mismatch in the frequency responses of the various sensors. We will be concerned with the second-order partial derivative  $\partial^2 p(0,0,0,t)/\partial x \partial y$ . The results of error analyses of the other mixed second-order partial derivatives would be analogous. Figure 13 shows the arrangement of the pressure sensors.

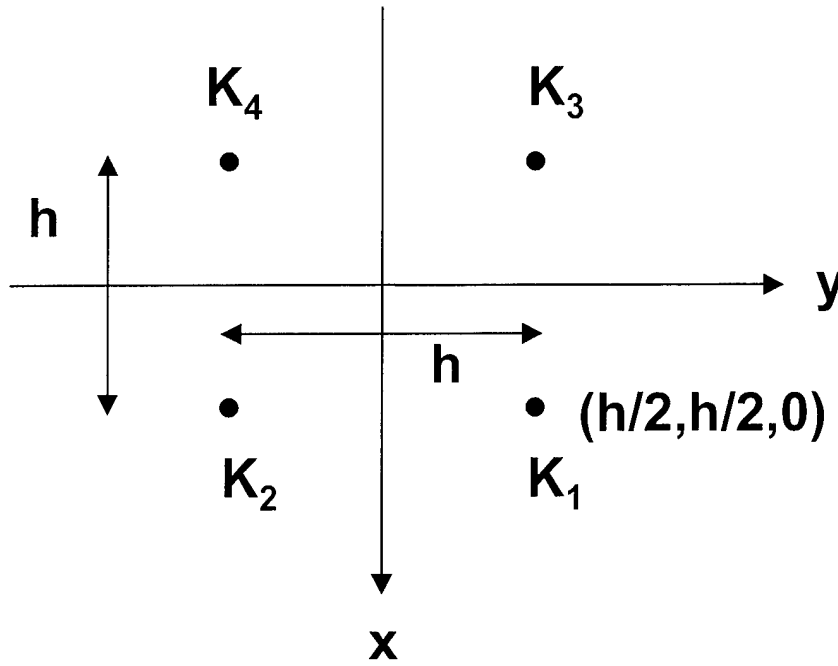


Figure 13. Arrangement of pressure sensors for the finite-difference approximation of the mixed second-order partial  $\partial^2 p / \partial x \partial y$  at the origin.

Starting with the estimation equation (13a) we would arrive at an equation analogous to (35), namely,

$$V_{xy}(\omega) = F(\omega) \frac{K_1 e^{j(k_x + k_y)h/2} - K_2 e^{j(k_x - k_y)h/2} + K_3 e^{j(-k_x + k_y)h/2} - K_4 e^{j(-k_x - k_y)h/2}}{h^2} \quad (42)$$

If  $K_4 = K_3 = K_2 = K_1$  (no mismatch), then (42) reduces to

$$V_{xy}(\omega) = -k_x k_y K_1 F(\omega) \text{sinc}(k_x h/2) \text{sinc}(k_y h/2) \quad (43)$$

The error  $\mathcal{E}$  takes on the form

$$\mathcal{E} = 20 \log |\text{sinc}(k_x h/2) \text{sinc}(k_y h/2)| \quad (44)$$

$\mathcal{E}$  approaches zero as  $h$  approaches zero. The problem is more complicated when the sensors are mismatched. The magnitude of (42) has the form

$$|V_{xy}(\omega)| = K_1 \frac{|F(\omega)|}{h^2} \sqrt{\underline{\mu}' \Gamma \underline{\mu}} \quad (45)$$

where

$$\underline{\mu} = \begin{bmatrix} 1 \\ K_2/K_1 \\ K_3/K_1 \\ K_4/K_1 \end{bmatrix} = \begin{bmatrix} 1 \\ \mu_2 \\ \mu_3 \\ \mu_4 \end{bmatrix} \quad (46)$$

$$\Gamma = \begin{bmatrix} 1 & -\cos(k_y h) & -\cos(k_x h) & \cos((k_x + k_y)h) \\ -\cos(k_y h) & 1 & \cos((k_x - k_y)h) & -\cos(k_x h) \\ -\cos(k_x h) & \cos((k_x - k_y)h) & 1 & -\cos(k_y h) \\ \cos((k_x + k_y)h) & -\cos(k_x h) & -\cos(k_y h) & 1 \end{bmatrix} \quad (47)$$

The error  $\mathcal{E}$  becomes

$$\mathcal{E} = 20 \log \left| \frac{\sqrt{\underline{\mu}' \Gamma \underline{\mu}}}{(k_x h)(k_y h)} \right| \quad (48)$$

When the vector  $\underline{\mu}$  contains all ones, (48) simplifies to (44). In order to gain some understanding of the behavior of (48), let us define

$$\text{dB}(i) \equiv 20 \log \left( \frac{K_i}{K_1} \right), \quad i = 2, 3, 4 \quad (49)$$

We will choose a positive number  $\text{dB}_{\max}$  and declare each  $\text{dB}(i)$  to be a random variable uniformly distributed on the interval  $(-\text{dB}_{\max}, +\text{dB}_{\max})$ . Once sample values are obtained, the sensor sensitivities are given by

$$K_i = K_1 10^{\left( \frac{\text{dB}(i)}{20} \right)}, \quad i = 2, 3, 4 \quad (50)$$

Figure 14 shows a plot of the error (48) versus the sensor separation in terms of a fraction of a wavelength for  $\text{dB}_{\max}$  going from 0.1 to 2 dB in steps of 0.1 dB. The values of  $\phi_r$  and  $\theta_r$  are  $90^\circ$  and  $45^\circ$ , respectively. Equations (49) and (50) were applied 100 times for each  $\text{dB}_{\max}$  and the maximum error plotted. Figure 14 reveals some important features of the estimation error. As the relative sensor separation  $h/\lambda$  becomes larger, the error is less sensitive to the degree of sensor mismatch. Note that at half-wavelength spacing the band of error between  $\text{dB}_{\max} = 0.1$  dB and  $\text{dB}_{\max} = 2$  dB is narrow. However for  $h/\lambda < 0.2$ , the relative error is highly sensitive to sensor mismatch, the error reaching unsatisfactory values very quickly. In summary, for small  $h/\lambda$  the error is sensor-mismatch limited and for large  $h/\lambda$  the error is sensor-spacing limited. It appears from Figure 14 that the sensor spacing should be somewhere in midrange. Figure 15 gives a

plot of relative estimation error in dB for sensor spacing from 0.2 to 0.5 wavelengths, and sensor mismatch parameter  $\text{dB}_{\max}$  of 0.5, 1.0, 1.5, and 2.0 dB.

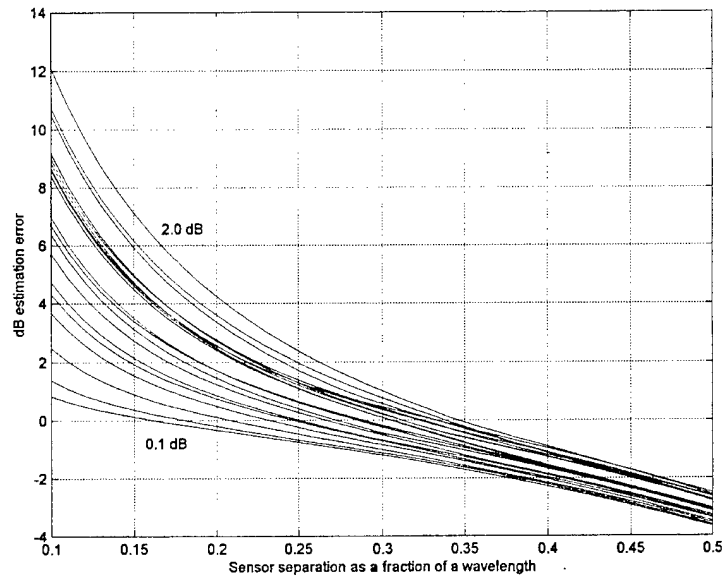


Figure 14. Error  $\epsilon$  with  $\text{dB}_{\max}$  going from 0.1 to 2 dB in steps of 0.1 dB and  $\phi_T = 90^\circ$  and  $\theta_T = 45^\circ$ .

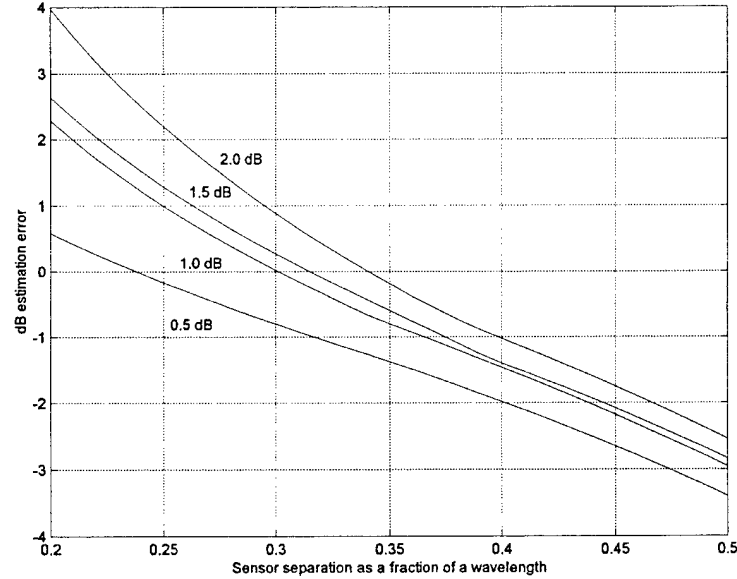


Figure 15. Error  $\epsilon$  with  $\text{dB}_{\max}$  of 0.5, 1.0, 1.5, and 2.0 dB and  $\phi_T = 90^\circ$  and  $\theta_T = 45^\circ$

#### 4.4 Summary

This section has analyzed some of the errors that occur when finite-differences are used to estimate the first-order and second-order partial derivatives of the acoustic pressure. The errors considered are those caused by a (1) finite, nonzero spacing  $\Delta x$  between sensors and (2) an amplitude mismatch among the composite frequency responses of the various sensors. Expressions for these errors were derived and plots were generated that illustrated the dependency of error-behavior on relative sensor spacing and dB-mismatch.

This section ends by describing pictorially the statistical behavior of the estimation error. Let  $\phi_r = 90^\circ$  and  $\theta_r = 45^\circ$ . Let us first focus on estimating  $\partial^2 p(0,0,0,t)/\partial x \partial y$ . Figure 16 shows a histogram of the estimation error (equation (48)) at a sensor spacing of 0.1 wavelengths. All of the sensors were assumed to be within  $\pm 0.2$  dB of each other (a uniform probability distribution for each  $\mu_j$  was assumed). The histogram represents a compilation of 2000 sample realizations. Also illustrated in Figure 16 is the mean value and standard deviation of the estimation error for sensor spacing from 0.1 to 0.5 wavelengths. At a spacing of 0.1 wavelengths, the mean error is about 0.25 dB. However, the standard deviation is 1 dB. Note that as the spacing increases, the mean error increases, whereas the standard deviation decreases.

Figure 17 contrasts the estimation of the first-order partial derivative  $\partial p(0,0,0,t)/\partial x$  and the second-order partial derivative  $\partial^2 p(0,0,0,t)/\partial x^2$ . For both cases,  $\phi_r = 90^\circ$  and  $\theta_r = 0^\circ$ . Observe the plots in the upper portion of Figure 17. The mean error (in estimating the second-order partial, refer to equation (41)) at the right is twice the mean error (in estimating the first-order partial) at the left. The lower portion of Figure 17 shows the standard deviation of both cases. In the first-order partial case, the standard deviation is constant with respect to sensor spacing and has a small value of 0.0571. In the second-order partial case, the standard deviation decreases exponentially from 0.66 at a spacing of 0.1 wavelengths to 0.065 at a spacing of 0.5 wavelengths. At a sensor spacing of 0.1 wavelengths, the mean error in estimating the first-order partial is  $-0.14$  dB and the mean error in estimating the second-order partial is  $-0.28$  dB. Note that at small values of sensor spacing, the standard deviation of the error in estimating the second-order partial is large as compared to the mean value of the error. The opposite is true for the estimation of the first-order partial derivative. That is, the standard deviation of the error is small as compared to the mean value of the error. From Figures 16 and 17, we conclude that finite-differences can be utilized effectively in estimating the gradient of the pressure, but confidence in finite-difference techniques decreases significantly when they are used to estimate the Hessian of the pressure. It is therefore recommended that an acoustic dyadic sensor be realized with 18 accelerometers and a pressure sensor at the origin. This will eliminate the gradient estimation error and significantly reduce the Hessian estimation error, since the Hessian can now be estimated by first-order finite difference approximations. (Refer to equations (14), (15) and (16)).

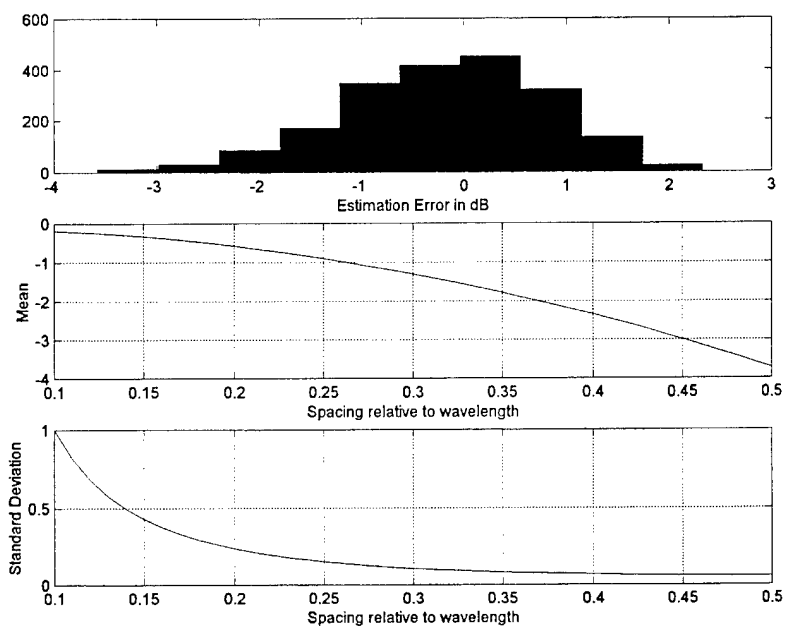


Figure 16. Statistical behavior of the error in estimating the mixed second-order partial derivative (with respect to  $x$  and  $y$ ) at the origin.

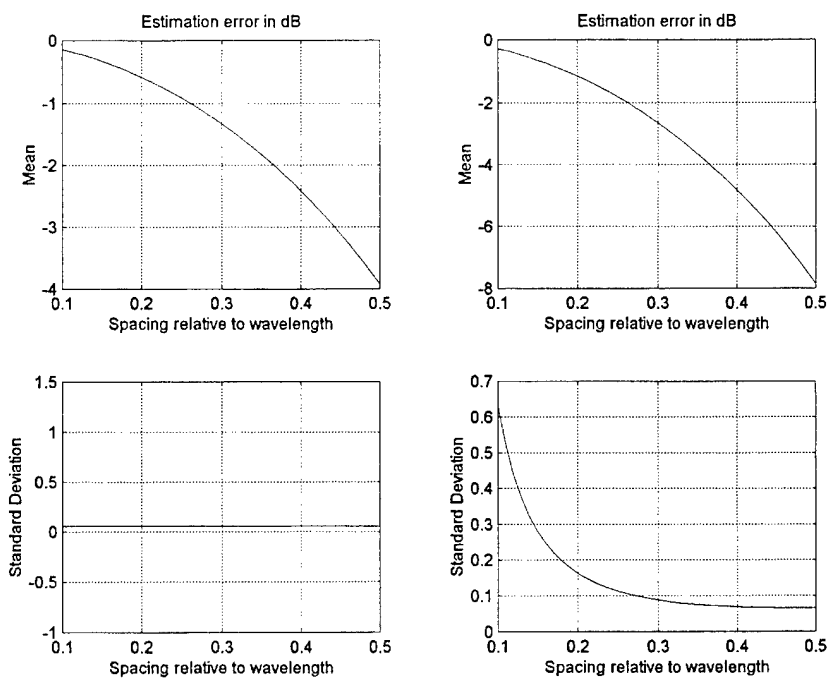


Figure 17. Statistics of the error in estimating the first-order (shown at the left) and pure second-order (shown at the right) partial derivatives of the pressure at the origin.

## 5.0 Multichannel Filtering and Directional Acoustic Sensors

For the purposes of this section, it is convenient to deal with the temporal Fourier transform of the Taylor series (8). Generalizing (8) in the frequency domain we obtain

$$\hat{P}(\omega, \vec{r}) = W_0(\omega, \vec{r})P(\omega, \vec{r}_0) + \vec{W}_1(\omega, \vec{r}) \cdot \nabla P(\omega, \vec{r}_0) + \vec{W}_2(\omega, \vec{r}) \cdot \nabla \nabla P(\omega, \vec{r}_0) \cdot \vec{W}_2(\omega, \vec{r}), \quad (51)$$

where we have retained only the first three terms of the series (dyadic sensor) and the weights  $W_0$ ,  $\vec{W}_1$  and  $\vec{W}_2$  are chosen such that the right side of (51) is consistent with the Taylor series approximation of the pressure field. Specifically,  $W_0 = 1$ ,  $\vec{W}_1 = \vec{r} - \vec{r}_0$  and  $\vec{W}_2 = (\vec{r} - \vec{r}_0)/\sqrt{2}$  are the only weights that allow (51) to be a Taylor series extrapolation of the pressure field by a dyadic sensor.

It is important to note that (51) is valid for any analytic acoustic wave field. For the special case of an arbitrary plane wave we have that

$$P(\omega, \vec{r}_0) = F(\omega) e^{j\vec{k} \cdot \vec{r}_0} \quad (52a)$$

$$\nabla P(\omega, \vec{r}_0) = jP(\omega, \vec{r}_0) \vec{k} \quad (52b)$$

$$\nabla \nabla P(\omega, \vec{r}_0) = -P(\omega, \vec{r}_0) \vec{k} \vec{k} \quad (52c)$$

where the quantity  $\vec{k} \vec{k}$  is a dyadic and is equivalent to the rank 1 matrix  $\underline{k} \underline{k}^T$  where

$$\underline{k} = \begin{bmatrix} k_x \\ k_y \\ k_z \end{bmatrix} \quad (53)$$

Without loss of generality, we can let  $\vec{r}_0 = (0,0,0)$  in (52). The substitution of (52) into (51) gives

$$\hat{P}(\omega, \vec{r}) = P(\omega, \vec{0}) g(\vec{k}, \vec{r}) \quad (54)$$

where

$$g(\vec{k}, \vec{r}) = 1 + j\gamma - \frac{1}{2}\gamma^2 \quad (55)$$

$$\gamma \equiv \vec{k} \cdot \vec{r} = 2\pi \frac{r}{\lambda} \hat{n} \cdot \hat{r} \quad (56)$$

The magnitude of (55) is



$$|g(\vec{k} \cdot \vec{r})| = \sqrt{1 + \frac{\gamma^4}{4}} \quad (57)$$

Equation (54) is in actuality an estimation provided by a dyadic sensor of the temporal Fourier transform of the pressure of a plane wave at the field point specified by the vector  $\vec{r}$ . The quality of the estimation would depend on the value of  $r/\lambda$ , where  $r$  is the distance of the field point from the origin and  $\lambda$  is the wavelength. Indeed, from (52) and (54) we can write

$$\epsilon_p = 20 \log \left| \frac{\hat{P}(\omega, \vec{r})}{P(\omega, \vec{r})} \right| = 20 \log |g(\vec{k} \cdot \vec{r})| \quad (58)$$

The magnitude of the  $g$  function is seen to define the dB error resulting from estimating  $P(\omega, \vec{r})$  by means of replacing the Taylor series by a Taylor polynomial of degree 2.

Figure 18 contains several normalized polar plots of  $10^{\epsilon_p/10} = |\hat{P}/P|^2$  plotted as a function of  $\theta_s$  for  $\phi_T = \phi_S = 90^\circ$  and  $\theta_T = 0^\circ$  where the angles  $\phi_S$  and  $\theta_S$  appear in the vector

$$\hat{r} = \sin \phi_S \cos \theta_S \hat{x} + \sin \phi_S \sin \theta_S \hat{y} + \cos \phi_S \hat{z} \quad (59)$$

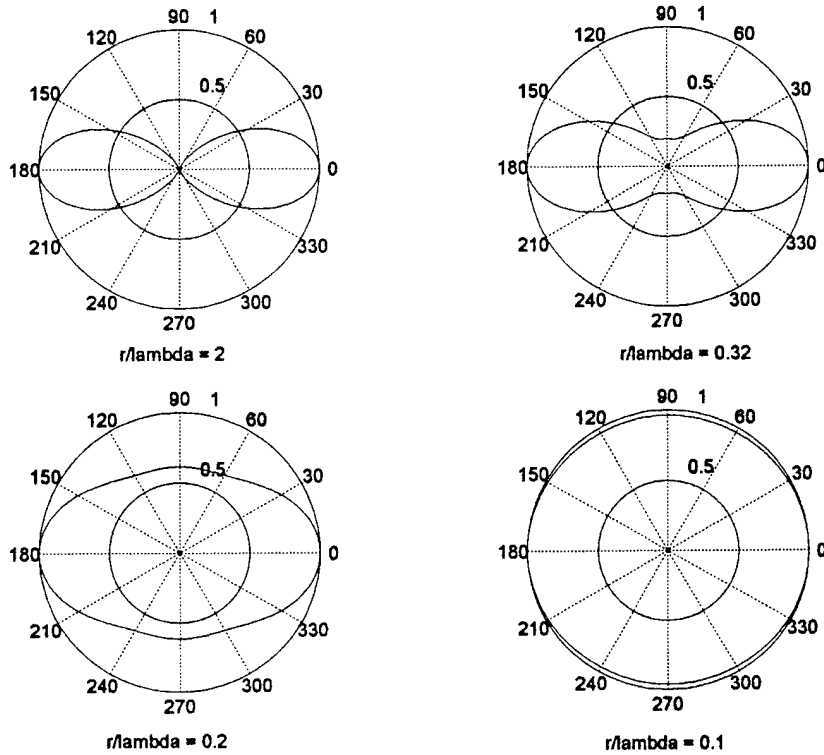


Figure 18. Polar plots of the normalized Taylor approximation error as a function of  $\theta_s$  for  $\phi_S = \phi_T = 90^\circ$  and  $\theta_T = 0^\circ$  and several values of  $r/\lambda$ .

The parameter  $r/\lambda$  takes on values of 2, 0.32, 0.2, and 0.1. The plots have been normalized so that the maximum value is unity. Observe that the polar plots in Figure 18 have the form of a beam pattern. As  $r/\lambda$  becomes smaller, the beam pattern approaches an omnidirectional pattern. The  $r/\lambda = 2$  pattern has a beam width of  $65.54^\circ$ . Equation (58) can be given two interpretations: (1) Taylor approximation error and (2) beam pattern. Thus, (54) can be interpreted as the generator of a beam pattern. In this interpretation the value of  $r$  is not driven by the need for an acceptable error bound on the estimate of  $P(\omega, \vec{r})$ . The variable  $r$  simply becomes a parameter in the forming of a beam and the function  $g(\vec{k}, \vec{r})$  can be interpreted as a discriminative function. The vector  $\hat{r}$  in (56) becomes a steering vector and we are now interested in the quality of discrimination of the beam rather than the quality of estimation of  $P(\omega, \vec{r})$ .

From Figure 18 we see that there is an ambiguity in the beam patterns (presence of two peaks). Mathematically, this ambiguity is caused by the fact that (57) is an even function of  $\gamma$ . It would be beneficial to generate beam patterns that do not have this ambiguity. Beam pattern ambiguity can be eliminated or significantly reduced by picking other sets of weights in (51). However, by doing so, we no longer have a valid Taylor series. It is more correct to modify (51) to

$$B(\omega, \vec{r}) = W_0(\omega, \vec{r})P(\omega, \vec{r}_0) + \vec{W}_1(\omega, \vec{r}) \cdot \nabla P(\omega, \vec{r}_0) + \vec{W}_2(\omega, \vec{r}) \cdot \nabla \nabla P(\omega, \vec{r}_0) \cdot \vec{W}_2(\omega, \vec{r}) \quad (60)$$

where the function  $B(\omega, \vec{r})$  could represent the output of a frequency domain multi-channel filter with  $P(\omega, \vec{r}_0)$ ,  $\nabla P(\omega, \vec{r}_0)$  and  $\nabla \nabla P(\omega, \vec{r}_0)$  as the inputs. Refer to Figure 19 for a pictorial representation of this concept.



Figure 19. Multi-channel Filtering and Directional Acoustic Sensors

Thus, (60) is a generalization of (51) and can be viewed as a multi-channel filtering approach to directional sensors. Consider the following set of weights:

$$\begin{aligned} W_0(\omega, \vec{r}) &= 1 \\ \vec{W}_1(\omega, \vec{r}) &= \alpha \frac{c}{j\omega r} \vec{r} \\ \vec{W}_2(\omega, \vec{r}) &= \sqrt{\beta} \frac{c}{j\omega r} \vec{r} \end{aligned} \quad (61)$$

where  $\alpha$  and  $\beta$  are two parameters that may be a function of frequency. The substitution of (61) into (60) results in

$$B(\omega, \vec{r}) = P(\omega, \vec{0})g(\hat{n}, \hat{r}) \quad (62)$$

where

$$g(\hat{n}, \hat{r}) = 1 + \alpha(\hat{n} \cdot \hat{r}) + \beta(\hat{n} \cdot \hat{r})^2 \quad (63)$$

We could select the weights in (63) to steer the beam of the directional sensor so that we have maximum sensitivity in the look direction and place a null in another direction. Further, we could select the weights so that the directional sensor produces a beam pattern that results in maximum array gain against isotropic noise [14]. Figure 20 shows the two weight-selection criteria for the vector sensor. The maximum-array gain case of Figure 20(a) corresponds to  $\alpha = 3, \beta = 0$ , whereas the optimum-null case of Figure 20(b) corresponds to  $\alpha = 1, \beta = 0$ . Figure 21 does the same for the case of the dyadic sensor. The maximum-array gain case of Figure 21(a) corresponds to  $\alpha = -2, \beta = -5$ , whereas the optimum-null case of Figure 21(b) corresponds to  $\alpha = 2, \beta = 1$ . Observe that in each case, the ambiguity was eliminated or significantly reduced.

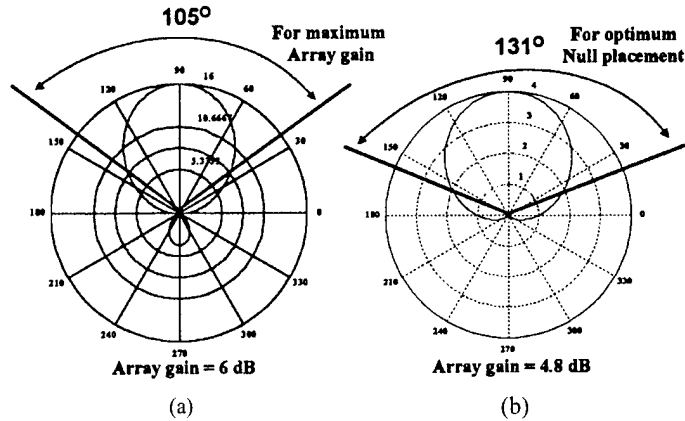


Figure 20. Selection of weights for a vector sensor. (a) For maximum array gain. (b) For optimum null placement.

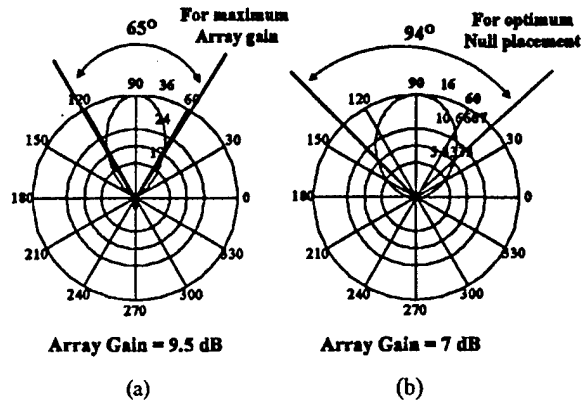


Figure 21. Selection of weights for a dyadic sensor. (a) For maximum array gain. (b) For optimum null placement.

## 6.0 Experimental Results Using a Partial Dyadic Sensor

A vector sensor placed at a point in space measures both the pressure and the gradient of the pressure at that point. A dyadic sensor also does this. In addition, it also measures all of the spatial second-order partial derivatives of the pressure at the point. This section will discuss a *partial* dyadic sensor. The dyadic sensor is *partial* in the sense that it only measures the spatial pure second-order partial derivatives of the pressure (i.e., the diagonal elements of the Hessian matrix (7)), not the mixed second-order partials. Figure 5 shows the placement of the components of the partial dyadic sensor. The components consist of a pressure sensor at the origin and six CAVES-type (flexural disk) accelerometers placed at the extremities of the three orthogonal lines in Figure 5. SITTEL CORPORATION used the services of EDO Electro-Ceramic Products, Salt Lake City, Utah to build the partial dyadic sensor illustrated in Figure 22. Figure 23 shows the support structure used to make beam pattern measurements. These measurements were performed at Seneca Lake in May 2001.

In section 6.1, we derive the theoretical beam patterns for the elements of the partial dyadic sensor and provide measured results from Seneca Lake to validate the theory. In section 6.2, we show how multi-channel signal processing of a vector sensor can be used to realize the performance of a dyadic sensor when the pressure field is assumed to be an arbitrary plane wave. We also provide experimental results to validate this claim.

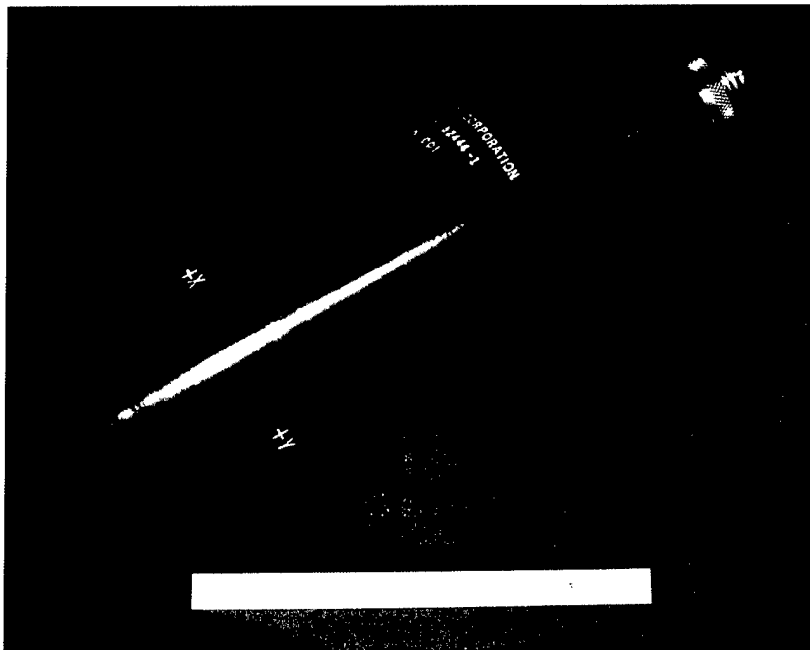


Figure 22. Partial dyadic sensor built by EDO Electro-Ceramic Products.

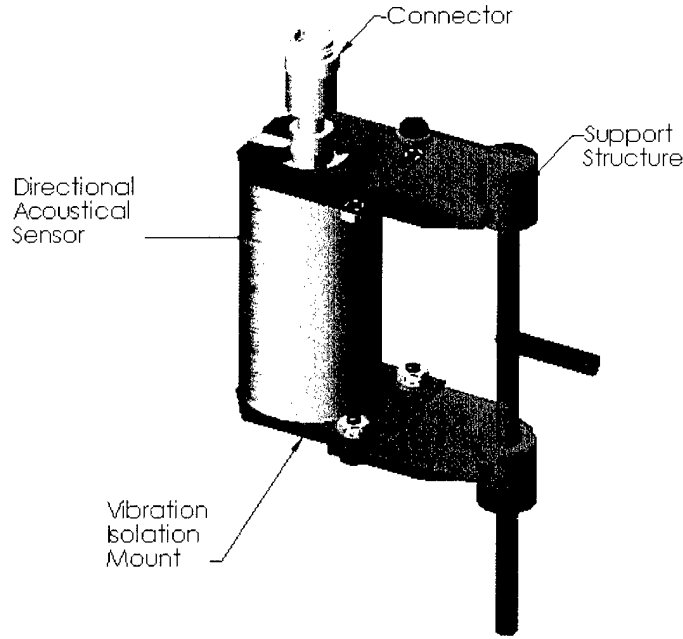


Figure 23. Support structure used for partial dyadic sensor.

### 6.1 Theoretical and Experimental Beam Patterns for a Partial Dyadic Sensor

The goal of this section is to discuss beam patterns produced by particular accelerometer components and certain combinations of accelerometer components of the EDO sensor. Specifically, we will focus on the lines labeled  $\partial^2 p / \partial x^2$  and  $\partial^2 p / \partial y^2$  in Figure 5. The accelerometer at the left extremity of the line  $\partial^2 p / \partial x^2$  will be referred to as the  $+x$  accelerometer, whereas the accelerometer at the right extremity will be called the  $-x$  accelerometer. Similarly, the accelerometer at the foremost extremity of the line  $\partial^2 p / \partial y^2$  will be referred to as the  $+y$  accelerometer, whereas the accelerometer at the rearmost extremity will be called the  $-y$  accelerometer. Before presenting empirical beam pattern measurements, it is necessary to first discuss the theoretical equivalents. It is well known in the theory of vector sensors, that the frequency-independent beam pattern of a single accelerometer follows a  $\cos \theta$  ( $+x$  or  $-x$  accelerometer) or  $\sin \theta$  ( $+y$  or  $-y$  accelerometer) pattern. We will derive the theoretical beam pattern for  $\partial a_x / \partial x$ , which can be approximated by the first-order finite difference of the  $+x$  and  $-x$  accelerometers. Let us begin with the relationship

$$\frac{\partial a_x}{\partial x} = -\frac{1}{\rho} \frac{\partial^2 p}{\partial x^2} \quad (64)$$

This relationship is valid for a homogeneous medium resulting in a constant  $\rho$ . For a sinusoidal plane wave of frequency  $\omega$ , (64) becomes

$$\frac{\partial a_x(t, \vec{r})}{\partial x} = \frac{k^2}{\rho} \sin^2 \phi_T \cos^2 \theta_T p(t, \vec{r}) \quad (65)$$

The mean-square value of (65) is

$$\overline{\left( \frac{\partial a_x(t, \vec{r})}{\partial x} \right)^2} = \kappa^2 \cos^4 \theta_T \quad (66)$$

where

$$\kappa = \frac{k^2}{\rho} \sin^2 \phi_T \overline{p^2(t, \vec{r})} \quad (67)$$

The parameter  $\kappa$  is kept constant by fixing the frequency  $\omega$  and the angle  $\phi_T$ . We generate a theoretical beam pattern for  $\partial a_x / \partial x$  by plotting (66) as a function of the angle  $\theta_T$ . Similarly, we generate a theoretical beam pattern for  $\partial a_y / \partial y$  by plotting

$$\overline{\left( \frac{\partial a_y(t, \vec{r})}{\partial y} \right)^2} = \kappa^2 \sin^4 \theta_T \quad (68)$$

as a function of the angle  $\theta_T$ .

A first-order finite difference of the  $+x$  and  $-x$  accelerometers was used to estimate the left side of (64). Figures 24 (a) and (b) give the empirical and theoretical beam patterns of both accelerometers at 1200 Hz. Both empirical patterns are close to the theoretical “ $\cos \theta$ ” pattern. Note the  $-25$  dB nulls in the empirical patterns. Figure 24 (c) consists of the empirical and theoretical patterns for  $\partial a_x / \partial x$ . The empirical pattern is close to the theoretical “ $\cos^2 \theta$ ” pattern. Note the  $-21$  dB nulls for the empirical pattern in contrast to the infinite nulls for the theoretical pattern. Pulsing a source at a fixed frequency of 1200 Hz, recording and processing data, and then rotating the vertical shaft in Figure 23 in the  $xy$  plane in order to achieve a different angle  $\theta_T$  generated the patterns for  $\partial a_x / \partial x$  and  $\partial a_y / \partial y$ , respectively. Figures 25 (a) and (b) give the empirical and theoretical beam patterns of the  $+y$  and  $-y$  accelerometers. Both empirical patterns are close to the theoretical “ $\sin \theta$ ” pattern. Note the  $-25$  dB nulls in the empirical patterns. Figure 25 (c) consists of the empirical and theoretical patterns for  $\partial a_y / \partial y$ . The empirical pattern is close to the theoretical “ $\sin^2 \theta$ ” pattern. Note the  $-21$  dB nulls for the empirical pattern in contrast to the infinite nulls for the theoretical pattern.

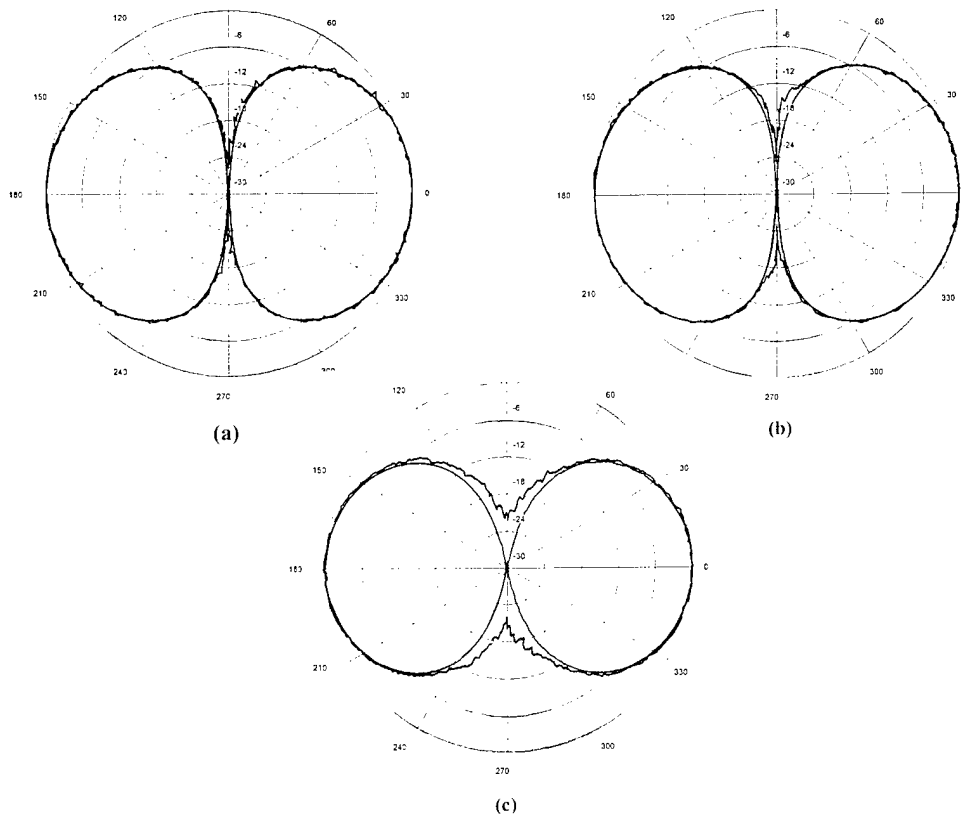


Figure 24. Empirical and theoretical beam patterns. (a) +x accelerometer (b) -x accelerometer (c) the difference between the +x and -x accelerometers.

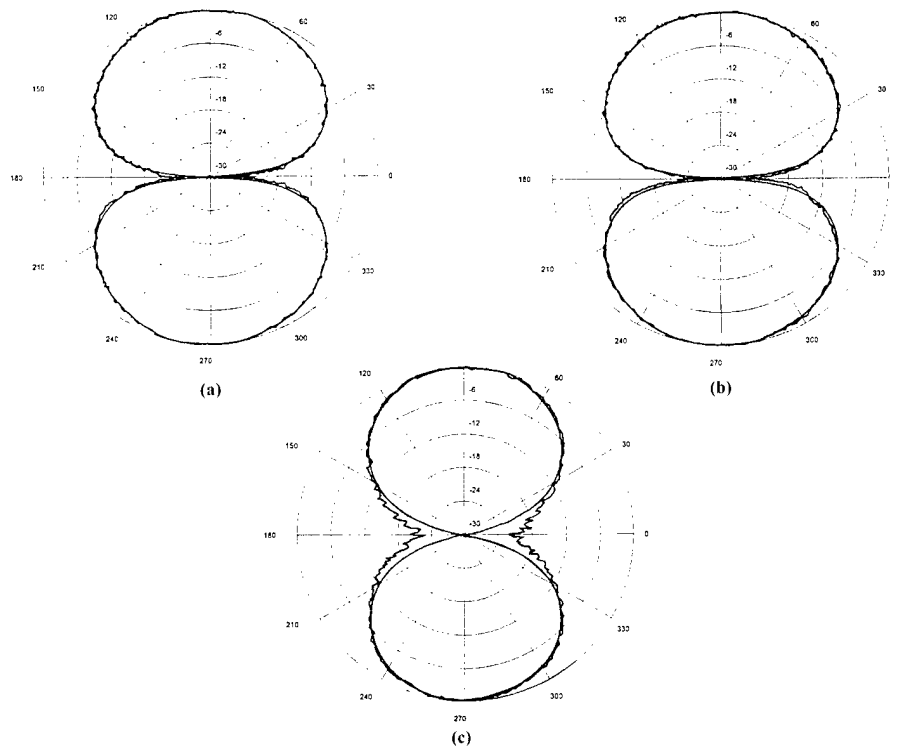


Figure 25. Empirical and theoretical beam patterns. (a) +y accelerometer (b) -y accelerometer (c) the difference between the +y and -y accelerometers.

## 6.2 Achieving Dyadic Sensor Performance by Multi-channel Processing of a Vector Sensor in a Plane Wave Field

In this section, we show how multi-channel signal processing of a vector sensor can be used to realize the performance of a dyadic sensor when the pressure field is assumed to be an arbitrary plane wave. We also provide experimental results to validate this claim.

First, consider the case where the pressure waveform is a sinusoidal (narrowband) plane wave having the form

$$p(x, y, z, t) = p(\vec{r}, t) = A \sin(\omega t + \zeta + \vec{k} \cdot \vec{r}) \quad (69)$$

The gradient and the Hessian of (69) at  $(x_0, y_0, z_0)$  are

$$\nabla p(x_0, y_0, z_0, t) = \underline{k} A \cos(\omega t + \zeta + \vec{k} \cdot \vec{r}_0) \quad (70)$$

$$\nabla \nabla p(x_0, y_0, z_0, t) = -\underline{k} \underline{k}' A \sin(\omega t + \zeta + \vec{k} \cdot \vec{r}_0) \quad (71)$$

where  $\underline{k}$  is the column vector of wavenumbers. Let us now place a vector sensor at the point  $(x_0, y_0, z_0)$ . This sensor measures

$$p(x_0, y_0, z_0, t) = A \sin(\omega t + \zeta + \vec{k} \cdot \vec{r}_0) \quad (72)$$

$$\underline{a}(x_0, y_0, z_0, t) = -\frac{1}{\rho} \underline{k} A \cos(\omega t + \zeta + \vec{k} \cdot \vec{r}_0) \quad (73)$$

where the column vector  $\underline{a}$  contain the acceleration components. From (73) we obtain the 3 x 3 matrix

$$\underline{k} \underline{k}' = \frac{2\rho^2}{A^2} \int \underline{a}(x_0, y_0, z_0, t) \underline{a}'(x_0, y_0, z_0, t) dt \quad (74)$$

Equations (70) and (71) can be expressed as

$$\nabla p(x_0, y_0, z_0, t) = -\rho \underline{a}(x_0, y_0, z_0, t) \quad (75)$$

$$\nabla \nabla p(x_0, y_0, z_0, t) = -\frac{2\rho^2}{A^2} p(x_0, y_0, z_0, t) \int \underline{a}(x_0, y_0, z_0, t) \underline{a}'(x_0, y_0, z_0, t) dt \quad (76)$$

The above pair of equations indicates that for time-harmonic plane wave fields, both the pressure gradient and the pressure Hessian can be determined by pressure and



acceleration measurements. A vector sensor located at  $(x_0, y_0, z_0)$  achieves these measurements.

Let us now consider an arbitrary (narrowband or broadband) plane wave. An arbitrary plane wave moving towards the origin can be written in the form

$$p(x, y, z, t) = f\left(t + \frac{\hat{n} \cdot \vec{r}}{c}\right). \quad (77)$$

It follows  $\nabla p$  and  $\nabla \nabla p$  have the values

$$\nabla p = \underline{n} \frac{1}{c} g\left(t + \frac{\hat{n} \cdot \vec{r}}{c}\right) \quad (78)$$

$$\nabla \nabla p = \underline{nn}' \frac{1}{c^2} h\left(t + \frac{\hat{n} \cdot \vec{r}}{c}\right) \quad (79)$$

where

$$\begin{aligned} g &= f' \\ h &= g' = f'' \end{aligned} \quad (80)$$

The Fourier transforms of (77), (78), and (79) are

$$F[p] = F(j\omega) \exp\left[j\omega \frac{\hat{n} \cdot \vec{r}}{c}\right] \quad (81)$$

$$F[\nabla p] = \underline{n} \frac{1}{c} j\omega F[p] \quad (82)$$

$$F[\nabla \nabla p] = -\underline{nn}' \frac{1}{c^2} \omega^2 F[p] \quad (83)$$

The Fourier transform of the acceleration is given by

$$F[\underline{a}] = -\frac{1}{\rho} F[\nabla \nabla p] = -\frac{1}{\rho c} \underline{n} j\omega F[p] \quad (84)$$

Multiplying (84) by the transpose of its conjugate results in

$$F[\underline{a}] F^{*'}[\underline{a}] = \frac{1}{(\rho c)^2} \underline{nn}' \omega^2 |F[p]|^2 \quad (85)$$

Equation (85) leads to an expression for  $\underline{nn}'$ , namely,

$$\underline{nn}' = (\rho c)^2 \frac{\int F[\underline{a}] F^{*1}[\underline{a}] d\omega}{\int \omega^2 |F[p]|^2 d\omega} \quad (86)$$

The quantities  $\nabla p$  and  $\nabla\nabla p$  can be expressed in terms of the pressure and acceleration as follows:

$$F[\nabla p] = -\rho F[\underline{a}] \quad (87)$$

$$F[\nabla\nabla p] = -\rho^2 \omega^2 F[p] \frac{\int F[\underline{a}] F^{*1}[\underline{a}] d\omega}{\int \omega^2 |F[p]|^2 d\omega} \quad (88)$$

Equations (87) and (88) indicate that for an arbitrary plane wave field, both the pressure gradient and the pressure Hessian can be determined by pressure and acceleration measurements. A vector sensor located at  $(x_0, y_0, z_0)$  achieves these measurements.

Based on the above discussion, we can use equations (60) and (61) to construct a frequency domain multi-channel filter with  $P(\omega, \vec{r}_0)$ ,  $\nabla P(\omega, \vec{r}_0)$  and  $\nabla\nabla P(\omega, \vec{r}_0)$  as the inputs. ***In this way, we can obtain the performance of a dyadic sensor with vector sensor measurements.***

In order to validate this claim, tests were conducted at Seneca Lake during the period May 2001. A vector sensor was placed at the origin of a rectangular coordinate system and a 400 Hz acoustic target was placed at  $R_T = 130 \text{ ft.}$ ,  $\theta_T = 0^\circ$ ,  $\phi_T = 90^\circ$  relative to the vector sensor (refer to Figure 1). Figure 26 shows a contour plot of the mean-squared value of (60) as a function of frequency and azimuth with  $\beta = 0$  (a vector sensor). This is the Frequency-Azimuth (FRAZ) display for a vector sensor. The weights of the multi-channel filter ( $\alpha = 3, \beta = 0$ ) were chosen so that the vector sensor beam would achieve maximum array gain against isotropic noise. Figure 27 shows the FRAZ display that results when the weights of the multi-channel filter ( $\alpha = -2, \beta = -5$ ) were chosen so that the equivalent dyadic sensor beam would achieve maximum array gain against isotropic noise. A comparison of Figures 26 and 27 shows the spatial filtering improvement when using the extra estimate of (88) to achieve dyadic performance from a vector sensor.

Using the same test set-up as above, a 1300 Hz interfering source was placed at  $R_T = 222 \text{ ft.}$ ,  $\theta_T = 225^\circ$ ,  $\phi_T = 19^\circ$  relative to the vector sensor, so now we have a 400 Hz target and a 1300 Hz interferer simultaneously radiating energy toward the vector sensor. Once again, a comparison of Figures 28 and 29 shows the significant improvement of using the extra estimate of (88) to achieve dyadic performance from a vector sensor.

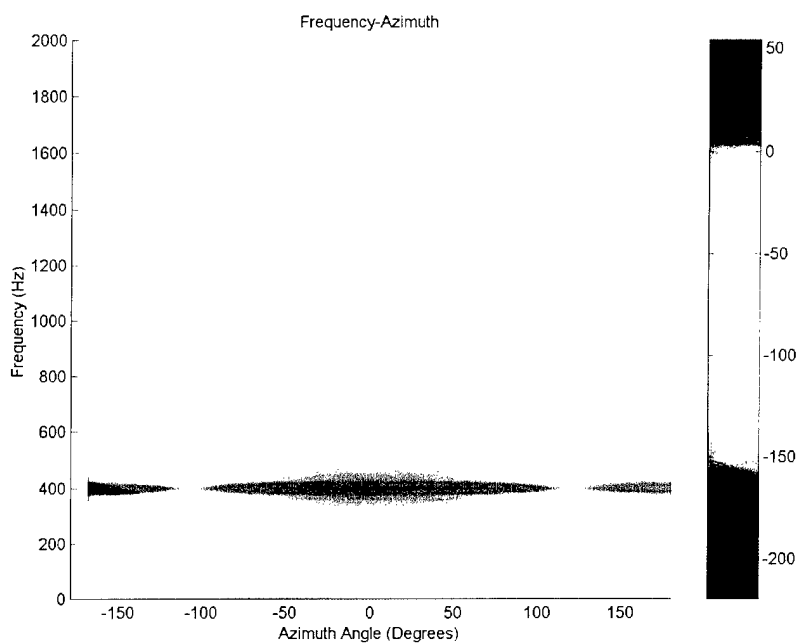


Figure 26. FRAZ display using vector sensor processing (single 400 Hz target located at  $r = 130$  ft,  $\theta_T = 0^\circ$ ,  $\phi_T = 90^\circ$ ).

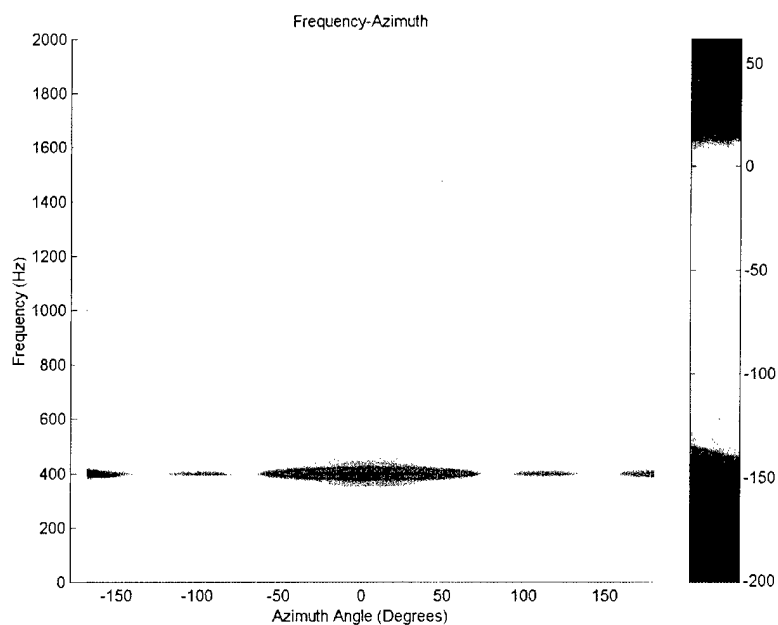


Figure 27. FRAZ display using dyadic sensor processing (single 400 Hz target located at  $r = 130$  ft,  $\theta_T = 0^\circ$ ,  $\phi_T = 90^\circ$ ).

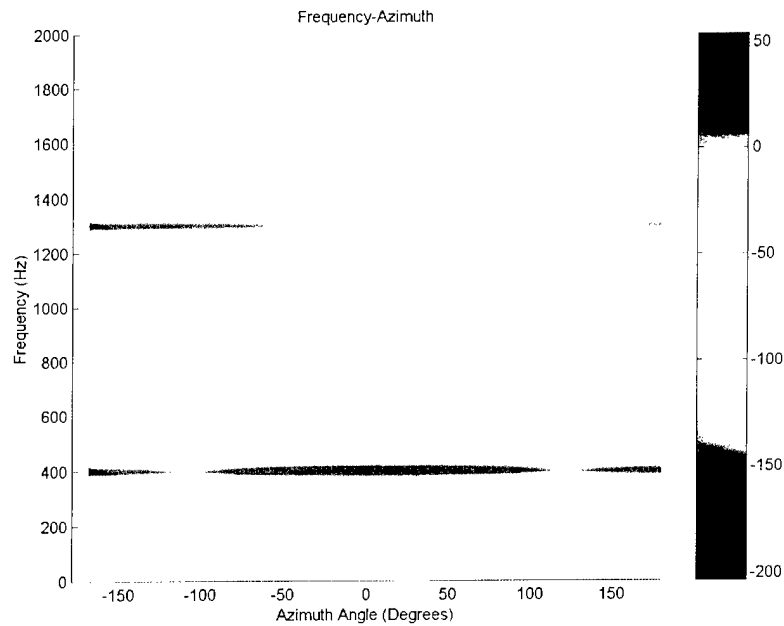


Figure 28. FRAZ display using vector sensor processing (400 Hz target located at  $r = 130$  ft,  $\theta_T = 0^\circ$ ,  $\phi_T = 90^\circ$  and 1300 Hz interferer located at  $r_I = 222$  ft,  $\theta_I = 225^\circ$ ,  $\phi_I = 19^\circ$  ).

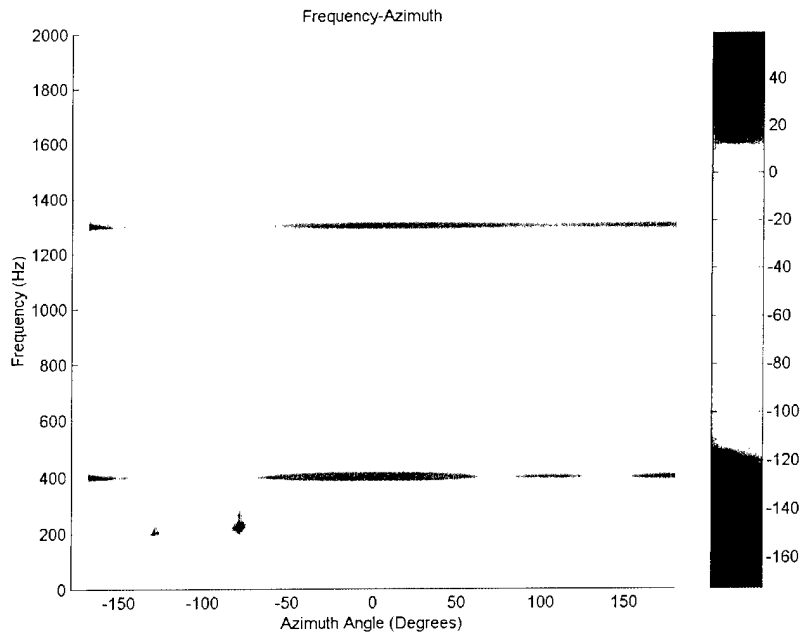


Figure 29. FRAZ display using dyadic sensor processing (400 Hz target located at  $r = 130$  ft,  $\theta_T = 0^\circ$ ,  $\phi_T = 90^\circ$ , and 1300 Hz interferer located at  $r_I = 222$  ft,  $\theta_I = 225^\circ$ ,  $\phi_I = 19^\circ$  ).

## 7.0 Effects of Quantization and Wide Band Noise on Finite Differences Between Two Accelerometers

This section analyzes the effects of quantization and wide band noise on the finite differences between sinusoidal signals received from two accelerometers spaced three to six inches apart. The noise bandwidth is 2000 Hz and is comprised of the following three components:

- (1) Ambient Ocean noise
- (2) Preamplifier noise
- (3) Analog to Digital Converter (ADC) quantizing noise.

Ambient noise ranges from the maximum acceptable noise as shown in the NUWC Vector Sensor Specifications dated 03 Feb 2000, to a value 40dB higher. An accelerometer sensitivity of  $-18 \text{ dBV/g}$  is used. Preamplifier noise is  $-166 \text{ dBV}/\sqrt{\text{Hz}}$ , which is equivalent to the noise floor of a SITTEL CORPORATION signal conditioner. ADC quantizing noise is 10.8dB below the least significant bit (LSB) level or quantizing

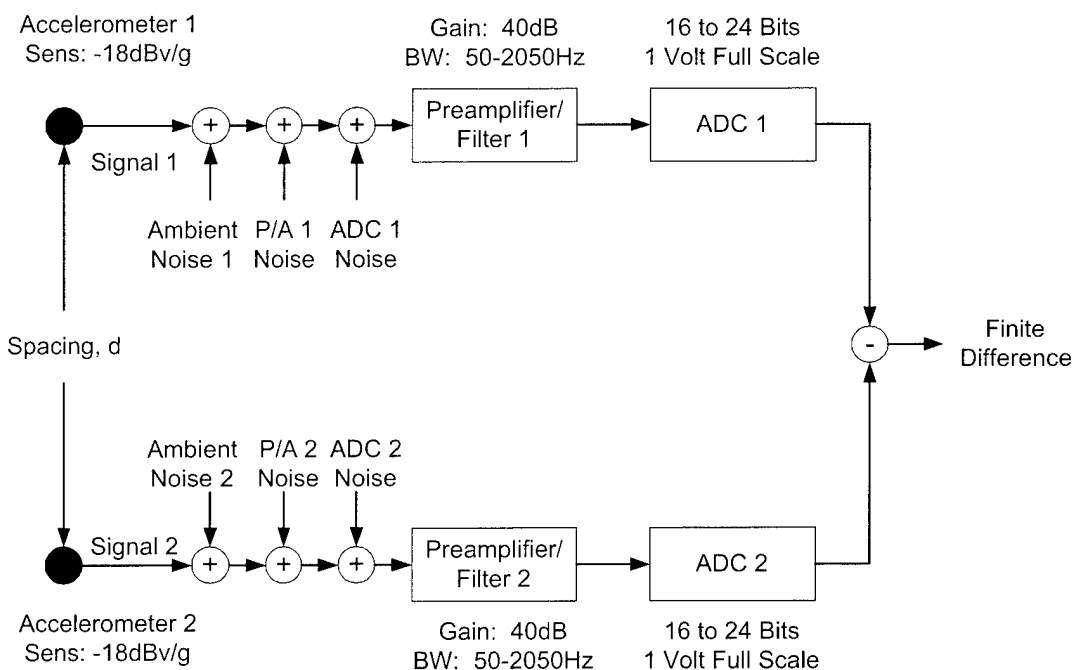


Figure 30. Modeling Setup

step size of the ADC. For an N-bit, bipolar ADC with full-scale amplitude of  $\pm F_s$ , the LSB level is  $F_s/2^{(N-1)}$ . The analysis uses both a 16-bit ADC and 24-bit ADC to observe the effects of quantizing step size on the finite difference errors. Figure 30 shows the modeling setup used for the analysis.

The analysis is comprised of the following four parts:

**Part 1.** The signal frequency is set at 50Hz, which is considered to be worst case since the finite differences are the smallest at the lowest signal frequencies within the band with fixed accelerometer spacing. Noise is considered to be uncorrelated between accelerometers. Accelerometer spacing is 3 inches and 6 inches. The RMS value of the composite noise ranges from 1 LSB to 100 LSB's for the 16-bit ADC and from 256 LSB's to 25,600 LSB's for the 24-bit ADC with the sinusoidal signal levels, in each case, ranging from 0dB to +50dB above the composite noise level. The signals are assumed to be plane wave and arrive along the axis formed by the two accelerometers.

**Part 2.** The signal frequency is set at 50Hz. Noise is uncorrelated between accelerometers. Accelerometer spacing is 3 inches and 6 inches. The RMS value of the composite noise ranges from 1 LSB to 100 LSB's for the 16-bit ADC and from 256 LSB's to 25,600 LSB's for the 24-bit ADC with the sinusoidal signal levels, in each case, ranging from 0dB to +50dB above the composite noise level. The signals are assumed to be plane wave and arrive along the axis formed by the two accelerometers. The signal is sensed with 2 accelerometer sets and averaged to determine improvement in errors due to averaging.

**Part 3.** The signal frequency is set at 50Hz. The noise correlation coefficient between accelerometers ranges from 0% to 95% to determine the improvements in finite difference errors due to correlated noise. The noise and signal attributes are as described in part 1 and part 2. A 16-bit ADC converter is used with 3-inch spacing between accelerometers. With close accelerometer spacing, ambient noise is likely to be correlated as described in Appendix A.

**Part 4.** The signal frequency varies from 50Hz to 2000Hz with a constant accelerometer spacing of 3 inches. Improvement is expected at higher frequencies due to greater finite differences. The ADC is set at 16 Bits with the input noise level set at 10dB above the LSB. The signal-to-noise ratio varies from 0dB to 50dB.

**Conclusions.** It is feasible to measure finite differences of 50Hz sinusoidal signals, in the presence of wide band noise, emanating from accelerometers with 3-inch spacing between accelerometers. When input signal plus noise levels are large enough to dither the ADC, the analysis shows that the errors depend upon the signal to noise ratio. An acceptable dithering level is 10dB or greater relative to the LSB of the ADC. At this level, there is no difference in error performance of a 16-bit ADC and a 24-bit ADC. Normalized errors are the difference between the perturbed finite difference and actual finite difference divided by the actual finite difference.

For a 50Hz signal from 2 accelerometers spaced 3 inches apart, with wide band noise uncorrelated between accelerometers, a SNR of 30dB is required to obtain a normalized average RMS error of 10%. The normalized average RMS error is the square root of the normalized mean square error averaged over a cycle of signal frequency. For a normalized maximum RMS error of 10%, the SNR must be in excess of 50dB. The normalized maximum RMS error is the square root of the maximum normalized MSE

within a cycle of signal frequency. In this analysis, the maximum MSE occurs at the peak of the sinusoidal signal where the minimum finite difference occurs. The minimum finite difference is defined as  $A*(1-\cos(\Delta\theta))$  where  $A$  is the peak signal amplitude and  $\Delta\theta$  is equal to  $2*\pi*d/\lambda$ , with  $d$  equal to the distance between accelerometers and  $\lambda$  equal to the wavelength. A SNR of 36dB is required for a normalized maximum RMS error equal to the minimum finite difference.

The analysis has shown that increasing the spacing between the accelerometers results in lower errors for the same signal frequency. At 50Hz, a 6dB improvement is realized by 6-inch spacing over 3-inch spacing.

The analysis has shown that averaging the finite differences of 2 sets of accelerometers looking at the same signal results in 3dB error improvement as long as the noise is uncorrelated between sets of accelerometers.

The analysis has shown that lower errors occur when the noise between accelerometers is correlated. The improvement is 7dB from 0% correlation to 90% correlation at a given SNR. The actual noise correlation is not known but is expected to be high due to the close spacing of the accelerometers.

Finally, the analysis has shown that 50Hz has the worst case errors. The errors for 3-inch spacing improve at higher frequencies. For frequencies up to 500Hz, the error improvement is 6dB per octave of frequency. For frequencies above 500Hz, the improvement is substantial, although less than 6dB per octave.

**Analysis.** A Monte Carlo analysis was used to compute the difference error due to noise and quantizing effects. A signal cycle was divided into 400 phases with each phase equivalent to the phase shift between accelerometers. The finite difference is the difference in instantaneous amplitudes between 2 adjacent phases of the signal. The mean square error (MSE), between the finite difference corrupted by noise and ADC effects, and the actual finite difference, was computed at each of the 400 phases using 2048 sample functions of noise at each ADC input. The average MSE was then computed by averaging the MSE over a cycle of signal input and normalizing to the actual finite difference. Likewise the maximum MSE was computed by determining the maximum MSE over a cycle and normalizing to the actual finite difference. It is expected that the maximum error occurred at the minimum finite difference. As shown in Appendix A, the minimum finite difference is equal to  $A*(1-\cos(\Delta\theta))$ , where  $A$  is the peak signal amplitude and  $\Delta\theta$  is equal to  $2*\pi*d/\lambda$ , with  $d$  equal to the distance between accelerometers and  $\lambda$  equal to the wavelength. The maximum finite difference is equal to  $A*\sin(\Delta\theta)$ .

With 3 inch spacing, at 50Hz,  $\Delta\theta$  is equal to 0.9 degrees, and the minimum finite difference is equal to  $A*123*10^{-06}$ . The ratio of maximum to minimum finite difference is 127 or 42.1 dB. With 6 inch spacing, at 50Hz,  $\Delta\theta$  is equal to 1.8 degrees, and the minimum finite difference is equal to  $A*493*10^{-06}$ . The ratio of maximum to minimum

finite difference is 63 or 36.1 dB. The finite differences are directly proportional to frequency for a constant spacing between accelerometers.

### **Analysis Part 1**

Figures 31 and 32 show the normalized average MSE and maximum MSE, respectively, versus input noise level and signal to noise ratio (SNR) for a 16 bit ADC and 3-inch spacing. The minimum noise level is about 10dB above the ADC LSB. A 30dB SNR is required for a normalized MSE of 1%, which corresponds to a normalized RMS error of 10%. However, for a normalized maximum MSE of 1%, a SNR in excess of 50dB is required. A 36dB SNR is required for a normalized maximum MSE less than the minimum finite difference.

These plots show that the errors are constant with input noise levels and a function of only the SNR for input levels that are 10dB or more above the LSB of the ADC. The slight decrease of errors at levels below 10dB relative to the LSB, for SNR's 0dB to 30dB are unexplained and may be anomalies caused by small input levels relative to the ADC LSB. Since it is good practice to maintain minimum RMS noise into an ADC at a level 10dB or more above the LSB, the data below 10dB is ignored.

Figures 33 and 34 show the normalized average MSE and maximum MSE, respectively, versus input noise level and SNR for a 24 bit ADC and 3-inch spacing. The minimum noise level is about 48dB above the ADC LSB. It can be seen that the errors are equivalent to those of the 16 bit ADC with input noise 13dB or higher relative to the LSB.

It can be concluded that as long as the input RMS noise level is kept above the LSB of the ADC, the finite difference errors of a 16 bit ADC is comparable to those of a 24 bit ADC. A 30dB SNR is required to keep the average MSE below 10%. A 36dB SNR will keep the maximum MSE below the minimum finite difference.

Figures 35 and 36 show the average MSE and maximum MSE, respectively, for a spacing of 6 inches, with 50Hz input into a 16-bit ADC. As shown in the figures, the errors are 6dB lower than those with 3-inch accelerometer spacing are. This suggests that higher frequencies will have lower errors at 3-inch spacing. Errors as a function of frequency are addressed in part 4 of this analysis.

### **Analysis Part 2**

Figures 37 and 38 show the average MSE and maximum MSE, respectively, for a spacing of 3 inches, with 50Hz input into a 16-bit ADC with the finite differences obtained from an average of 2 accelerometer sets. As shown in the figures, the errors are 3dB lower than those obtained with a single set of accelerometers. This analysis shows that as long as the noise is uncorrelated between sets of accelerometers, an improvement in finite difference error can be realized by averaging.



### Analysis Part 3

Adding portions of uncorrelated noise from one accelerometer into the other accelerometer simulated correlated noise. Defining  $N1$  as the noise from accelerometer #1 and  $N2$  as the noise from accelerometer #2, the correlated noise inputs are defined as  $N1' = N1 + \alpha * N2$ , and  $N2' = \alpha * N1 + N2$ , where  $\alpha$  is a coefficient, less than unity defined by the correlation coefficient,  $\rho$ , as follows:  $\alpha = [1 - (1 - \rho^2)^{1/2}] / \rho$ . Figures 10 and 11 show the improvements in average MSE and maximum MSE, respectively, due to noise correlation. For noise correlated at 90%, a 7dB improvement is realized.

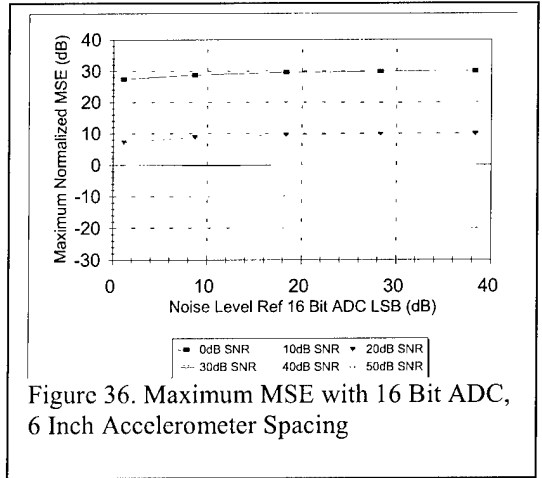
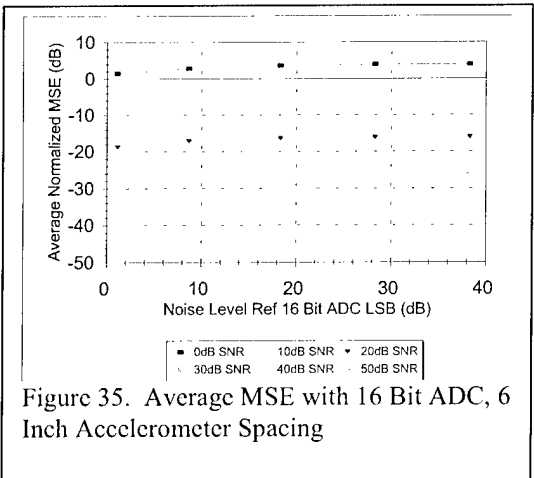
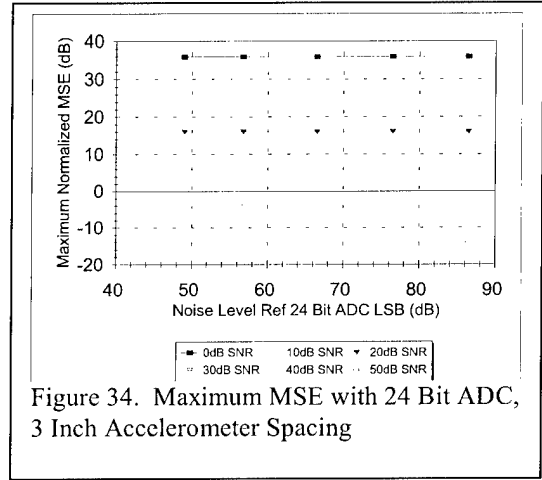
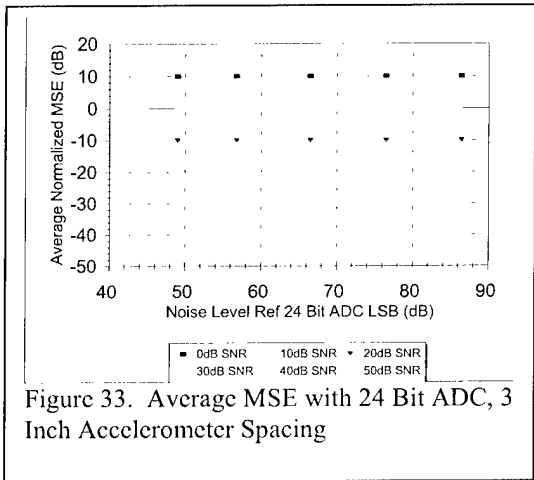
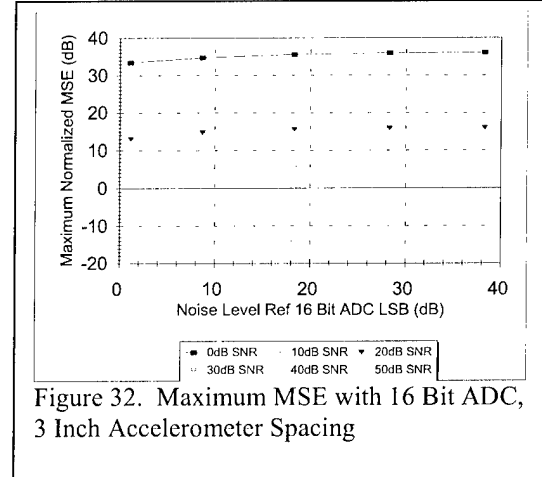
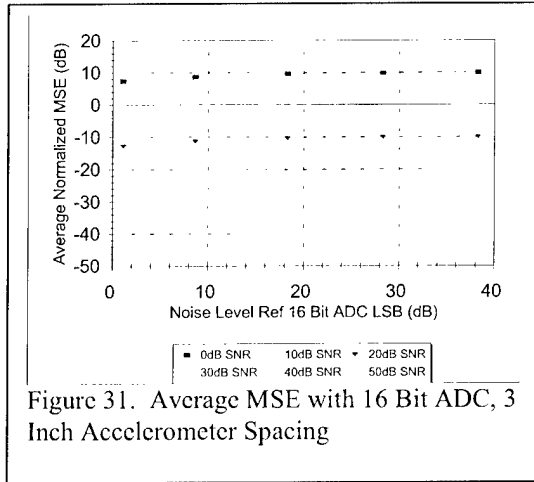
It can be concluded that noise correlation will result in an improvement in finite differences.

### Analysis Part 4

The signal frequency was varied from 50Hz to 2000Hz with a constant accelerometer spacing of 3 inches. The ADC was set at 16 Bits with the input noise level set at 10dB above the LSB. The signal-to-noise ratio was varied from 0dB to 50dB. Figures 41 and 42 show the improvements in average MSE and maximum MSE, respectively, as a function of frequency. At lower frequencies ( $f < 500$ ), the improvement is 6dB/octave of frequency. At higher frequencies, the improvement is less than 6dB/octave.

It can be concluded that 50Hz signals in the presence of uncorrelated wide band noise is the worst case for finite difference errors.

**Recommendations.** This analysis suggests that a dyadic sensor, covering the frequency band of 50 Hz to 2,050 Hz, can be built in a small package like the form factor of the existing DT 276 hydrophone (a 3-inch diameter by 6-inch long right circular cylinder). In order to fit the necessary accelerometers in this form factor, SITTEL recommends the use of singlecrystal or MEMS sensor technology. SITTEL is currently developing a complete dyadic sensor and signal processing design using this advanced sensor technology.



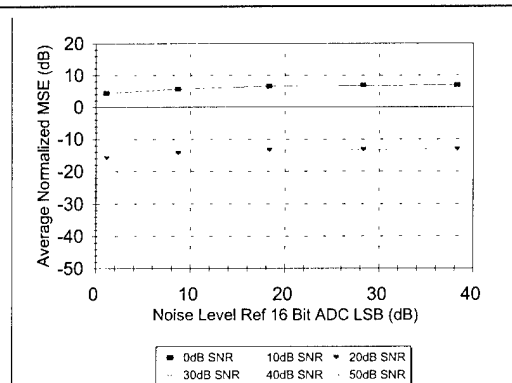


Figure 37. Average MSE with 16 Bit ADC, 3-Inch Accelerometer Spacing, and Average of 2 Accelerometer Sets

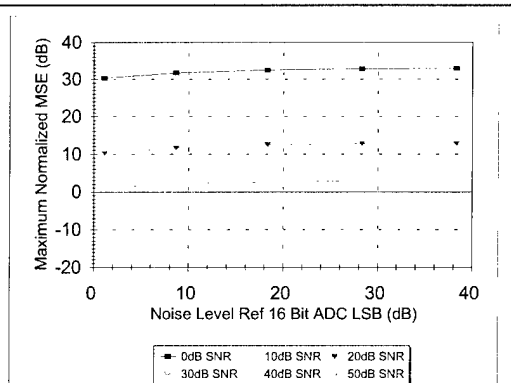


Figure 38. Maximum MSE with 16 Bit ADC, 3-Inch Accelerometer Spacing, and Average of 2 Accelerometer Sets

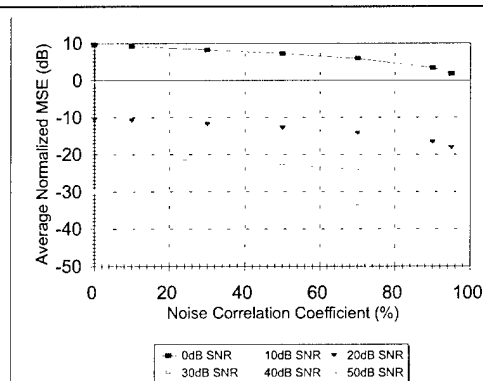


Figure 39. Average MSE with 16 Bit ADC as a Function of Noise Correlation

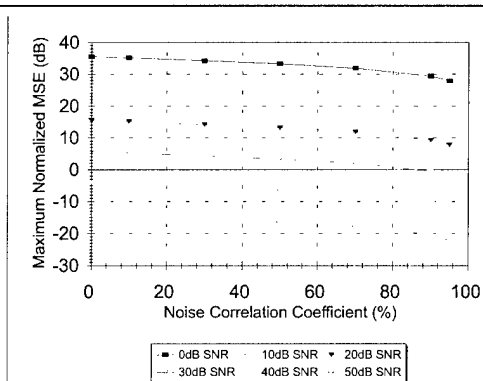


Figure 40. Maximum MSE with 16 Bit ADC as a Function of Noise Correlation

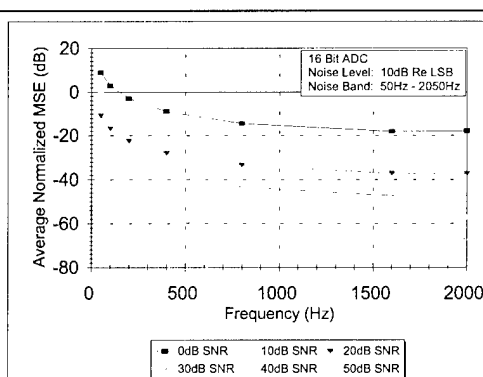


Figure 41. Average MSE with 16 Bit ADC and 3 Inch Accelerometer Spacing, as a Function of Frequency

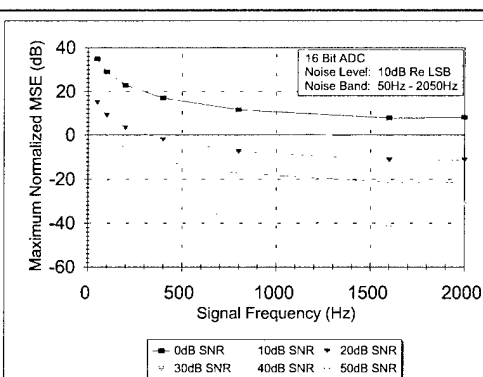


Figure 42. Maximum MSE with 24 Bit ADC and 3 Inch Accelerometer Spacing, as a Function of Frequency

## 8.0 Summary and Recommendations For Future Research

### 8.1 Summary

In Section 2.0, we formulated a rigorous mathematical framework for the general theory of directional acoustic sensors. Specifically, the number of terms in the multi-dimensional Taylor series expansion of the acoustic pressure field  $p(t, \vec{r})$  about some measurement point  $\vec{r}_0$  defines the order of the directional sensor. A **scalar acoustic pressure sensor** (e.g., a hydrophone) was defined as a directional acoustic sensor of order zero. This sensor only measures the scalar acoustic pressure  $p(t, \vec{r}_0)$  at the point  $\vec{r}_0$ ; its Taylor series about  $\vec{r}_0$  assumes that the acoustic pressure field  $p(t, \vec{r})$  about that point is independent of the field point  $\vec{r} = (x, y, z)$ . An **acoustic vector sensor** was defined as a directional acoustic sensor of order one. This sensor measures both  $p(t, \vec{r}_0)$  and the pressure gradient/vector  $\nabla p(t, \vec{r}_0)$  at the point  $\vec{r}_0$ ; its Taylor series about  $\vec{r}_0$  assumes that the acoustic pressure field  $p(t, \vec{r})$  about that point is a linear function of the field point  $\vec{r}$ . Similarly, an **acoustic dyadic sensor** was defined as a directional acoustic sensor of order two. This sensor measures  $p(t, \vec{r}_0)$ ,  $\nabla p(t, \vec{r}_0)$  and the dyadic  $\nabla \nabla p(t, \vec{r}_0)$  at the point  $\vec{r}_0$ ; its Taylor series about  $\vec{r}_0$  assumes that the acoustic pressure field  $p(t, \vec{r})$  about that point is a quadratic function of the field point  $\vec{r}$ .

Equation (8) is the pressure estimate generated by the dyadic sensor and is capable of extrapolating the acoustic pressure field beyond the measurement point  $\vec{r}_0$  so that it actually knows this field at every point inside a sphere of radius  $R = |\vec{r} - \vec{r}_0|$ , where  $R$  is defined by the type of directional sensor and the error associated with the extrapolation. The Taylor polynomial (8) is the formula used to do the wave field extrapolation with some specified error  $\varepsilon(t, \vec{r})$ . The normalized mean-squared value of  $\varepsilon(t, \vec{r})$  vs.  $R/\lambda$  is plotted in Figure 2. For a 10% pressure estimation error, the dyadic sensor measures the pressure field everywhere inside a sphere of radius  $R = \lambda/4$ . In this sense, the dyadic sensor is equivalent to a volumetric spherical array of pressure sensors. In practical terms, this means that for an acceptable pressure estimation error, a dense volumetric array of pressure sensors can be replaced by a sparse array of dyadic sensors.

In Section 3.0, we answered the question: *If three accelerometers and a pressure sensor (i.e., a vector sensor) can achieve a maximum array gain against isotropic noise of 6.0 dB, a question that naturally follows is how many more individual sensors (e.g., accelerometers and/or pressure sensors) must fit into a given sensor housing or form factor to improve upon the aforementioned directionality of the acoustic vector sensor?* Recall that the dyadic sensor measures  $p(t, \vec{r}_0)$ ,  $\nabla p(t, \vec{r}_0)$  and the dyadic  $\nabla \nabla p(t, \vec{r}_0)$  at the point  $\vec{r}_0$ . According to (6), (7), and (8), we must measure 13 terms involving the pressure and the first and second partial derivatives of the pressure. Due to the symmetry of the mixed partials in (7), the number of distinct terms reduces to 10. We demonstrated that these 10 terms can be estimated by 19 judiciously spaced pressure sensors, or 18

judiciously spaced accelerometers and 1 pressure sensor placed at the origin. Under these conditions, the dyadic sensor could achieve a maximum array gain against isotropic noise of 9.5 dB.

In Section 4.0, we examined the effects of finite-difference approximations on the estimation of the pressure gradient and Hessian (realization by pressure sensors) and also examined the effects of finite-difference approximations on the estimation of  $\nabla \bar{a}$  (realization by accelerometers). Specifically, this section analyzed some of the errors that occur when finite-differences are used to estimate the first-order and second-order partial derivatives of the acoustic pressure. The errors considered were those caused by a (1) finite, nonzero spacing  $\Delta x$  between sensors and (2) an amplitude mismatch among the composite frequency responses of the various sensors. Expressions for these errors were derived and plots were generated that illustrated the dependency of error-behavior on relative sensor spacing and dB-mismatch. From Figures 16 and 17, we conclude that finite-differences can be utilized effectively in estimating the gradient of the pressure, but confidence in finite-difference techniques decreases significantly when they are used to estimate the Hessian of the pressure. It is therefore recommended that an acoustic dyadic sensor be realized with 18 accelerometers and a pressure sensor at the origin. This will eliminate the gradient estimation error and significantly reduce the Hessian estimation error, since the Hessian can now be estimated by first-order finite difference approximations. (Refer to equations (14), (15) and (16)).

Section 5.0 discussed how the dyadic sensor can be viewed as a multi-channel filter. Refer to Figure 19. Specifically, equation (60) is the temporal Fourier transform of the output of the filter and the inputs to the filter are the temporal Fourier transforms of the pressure, pressure gradient and Hessian of the pressure. The filter weights  $W_0$ ,  $\bar{W}_1$  and  $\bar{W}_2$  can be functions of frequency and can be chosen so that the filter output is either an estimation of the pressure (a Taylor polynomial), a beam that achieves maximum array gain against isotropic noise, or a beam that can be shaped in some desired fashion, like placing a null in the beam pattern to spatially filter out an interfering source. With proper selection of the weights to achieve maximum array gain against isotropic noise, a dyadic sensor can produce a 65-degree beam (3-dB beam width). Under the same conditions, a vector sensor can produce a 105-degree beam.

The experimental results in Section 6.1 show that the elements of a partial dyadic sensor can produce acceptable beam patterns with nulls between -20 to -25 dB. The experimental results in Section 6.2 show that a dyadic sensor is a very effective multi-channel spatial filter.

Section 7.0 showed that first-order finite-difference approximations can be successfully performed in the presence of quantization and wide band noise effects. A worst-case analysis shows that using two accelerometers spaced 3 inches apart, one can achieve a normalized RMS error of 10% when attempting a first-order finite difference of a 50 Hz plane wave in a 2000 Hz band. This requires a signal-to-noise ratio (SNR) of at least 30 dB and assumes that the noise at each accelerometer is uncorrelated. This can be done using a 16-bit analog-to-digital converter (ADC). Further, for frequencies up to 2000 Hz, the required SNR drops off at about 6 dB per octave. This implies that the same 3-inch spaced accelerometers only need a SNR of 6 dB to achieve the same 10 % error for a first-order finite difference of an 800Hz plane wave.

## 8.2 Recommendations for Future Research

Based on the results in this report, SITTEL CORPORATION recommends the design, build and test of two complete dyadic sensors; each sensor using 18 underwater accelerometers and a single pressure sensor housed in the existing DT 276 form factor. In order to minimize the finite difference approximation errors and fit within the DT 276 form factor, SITTEL recommends the use of single crystal or MEMS technology to implement the accelerometers. SITTEL intends to perform extensive element pattern measurements associated with the complete Hessian matrix and compare these measurements to theoretical. For a general linear acoustic wave, we will perform extensive signal processing algorithms to show the improvement over the FY01 partial dyadic sensor and vector sensor. We will also demonstrate how two dyadic sensors can improve an intensity-based ranging algorithm using vector sensors. Further, we will show that for a single plane wave source, the outputs of a dyadic sensor can be processed in a triadic signal-processing algorithm to achieve triadic sensor performance.

## APPENDIX A

### 1. Finite Differences.

Define:  $S_1 = A \sin(\omega t)$   
 $S_2 = A \sin(\omega t - kd)$ , where:  $k = 2\pi/\lambda$  and  $d$  = spacing between accelerometers

Let:  $\omega t = \theta$  and  $kd = \Delta\theta$

Then:  $S_1 - S_2 = A(\sin\theta - \sin(\theta - \Delta\theta))$  which is maximum at  $\theta = 0$   
 And 0 at  $\theta = (\pi - \Delta\theta)/2$

The minimum step size used in this analysis occurs when  $\theta = \pi/2$ .  
 In this case  $S_1 - S_2 = A(1 - \cos(\Delta\theta))$

### 2. Effects of correlation.

Define:  $X_1 = S_1 + N_1$   
 $X_2 = S_2 + N_2$

With:  $\sigma_s^2$  = signal power, equal at both accelerometers  
 $\sigma_n^2$  = noise power, equal at both accelerometers  
 $\rho_s$  = signal correlation coefficient  
 $\rho_n$  = noise correlation coefficient

$$X_1 - X_2 = S_1 - S_2 + N_1 - N_2$$

$$\begin{aligned} \text{Output power} &= \langle (X_1 - X_2)^2 \rangle = \langle (S_1 - S_2)^2 \rangle + \langle (N_1 - N_2)^2 \rangle, \\ &= 2\sigma_s^2(1 - \rho_s) + 2\sigma_n^2(1 - \rho_n) \end{aligned}$$

Where  $\langle \rangle$  denotes expected value. Signal cross noise terms are equal to 0 since signal is uncorrelated to noise.

If signal is sinusoidal  $\rho_s = \cos(kd)$  or if broadband over range  $F_1$  to  $F_2$ ,  
 $\rho_s = \cos(\omega_0\tau) \sin(\pi B\tau) / (\pi B\tau)$ , with  $\omega_0 = \pi(F_2 + F_1)$ ,  $\tau = d/c$  and  
 $B = F_2 - F_1$

If noise is isotropic  $\rho_n = \sin(kd)/kd$ ,

For broadband noise:

$$\langle \rho_n \rangle = (kd_2 - kd_1)^{-1} \int_{kd_1}^{kd_2} d(kd) \sin(kd) / (kd), \text{ for } d = 3'', F_1 = 50, F_2 = 2050,$$

$\langle \rho_n \rangle = 0.976$  and  $2\sigma_n^2(1 - \langle \rho_n \rangle) / 2\sigma_n^2 = -16\text{dB}$  or noise is reduced by 16dB due to correlation

## REFERENCES

1. M. J. Berliner and J. F. Lindberg (eds.), "Acoustic Particle Velocity Sensors," Design, Performance and Applications," *AIP Conference Proceedings 368*, Mystic, Connecticut, 1995, American Institute of Physics Press, New York, 1996.
2. P. A. Wlodkowski and F. Schloss, "Advances in Acoustic Particle Velocity Sensorics," Proc. Of the Workshop on Directional Acoustic Sensors, Newport, RI, Sponsored by ONR and NUWC, 17-18 April, 2001.
3. P. David Baird, "EDO Directional Acoustic Sensor Technology," *Proc. Of the Workshop on Directional Acoustic Sensors*, Newport, RI, Sponsored by ONR and NUWC, 17-18 April, 2001.
4. A. Nehorai and E. Paldi, "Acoustic Vector-Sensor Array Processing", *IEEE Trans. On Signal Processing*, Vol. 42, No. 9, pp 2481-2491, Sept. 1994.
5. B. A. Cray and A. H. Nuttall, "A Comparison of Vector-Sensing and Scalar-Sensing Linear Arrays", NUWC-NPT Technical Report 10,632, 27 Jan 1997.
6. M. T. Silvia, R. E. Franklin and D. J. Schmidlin, "Signal Processing Considerations For a General Class of Directional Acoustic Sensors," Proc. Of the Workshop on Directional Acoustic Sensors, Newport, RI, Sponsored by ONR and NUWC, 17-18 April, 2001.
7. B. A. Cray, "Directional Acoustic Receivers: Signal and Noise Characteristics," Proc. Of the Workshop on Directional Acoustic Sensors, Newport, RI, Sponsored by ONR and NUWC, 17-18 April, 2001.
8. G. L. D'Spain, "The Vertical DIFAR Array", *presented at the Deployable Surveillance Workshop*, April 1992.
9. E. A. Robinson and M. T. Silvia, *Digital Foundations of Time Series Analysis: Volume 2: Wave Equation Space-Time Processing*, Holden-Day, Inc., San Francisco, 1981.
10. L. Camp, *Underwater Acoustics*, Wiley Interscience, NY, p. 53, 1970.



## DISTRIBUTION LIST

Addressee	No. of Copies
<b>Office of Naval Research (ONR)</b>	<b>7</b>
Steven E. Ramberg (Code 32)	
Nancy Harned (Code 321W)	
Frank Herr (Code 321)	
James McEachern (Code 321SS)	
Jan Lindberg (Code 321SS)	
Roy Elswick (Code 321SS)	
Donald Davison (Code 321SS)	
<b>Naval Undersea Warfare Center, Division Newport</b>	<b>4</b>
John Short (Code 20)	
Bruce A. Sandman (Code 01)	
James G. Kelly (Code 821)	
Benjamin A. Cray (Code 2133)	
<b>Defense Advanced Research Project Agency (DARPA)</b>	<b>2</b>
Wallace A. Smith (DSO)	
Douglas Cochran (DSO)	
<b>Advanced Systems Technology Office (ASTO)</b>	<b>2</b>
Peter Scala (ASTO)	
James Pierce (ASTO)	
<b>Naval Research Laboratory (NRL)</b>	<b>1</b>
Director (Code 5227)	
<b>SITTEL CORPORATION</b>	<b>3</b>
Dean J. Schmidlin	
Ryan Franklin	
Dennis Taylor	
<b>Defense Technical Information Center (DTIC)</b>	<b>2</b>
DODAAD CODE S47031	
<b>DCM (Van Nuys, CA)</b>	<b>1</b>